

Figure 5.5	Nusselt number distribution on the bottom plate of the channel with built-in circular tube	53
Figure 5.6	Limiting streamlines on a plane close to the bottom plate of a channel with built-in circular tube and a delta winglet-pair in common-flow-up configuration.	54
Figure 5.7	Streamline-plot on the horizontal midplane of a channel with built-in circular tube and delta winglet-pair in common-flow-up configuration	55
Figure 5.8	Streamline-plot on the vertical midplane of a channel with built-in circular tube and delta winglet-pair in common-flow-up configuration	56
Figure 5.9	Cross-stream velocity vectors at different x-locations behind the delta winglet-pair	57
Figure 5.10	Cross-stream velocity vectors at different x-locations behind the rectangular winglet-pair	58
Figure 5.11	Streamlines on the cross-stream planes at different x-locations behind the delta winglet-pair ( $b/D=1.67$ )	59
Figure 5.12	Streamlines on the cross-stream planes at different x-locations behind the rectangular winglet-pair ( $b/D=1.67$ )	60
Figure 5.13	Streamlines on the cross-stream planes at different x-locations behind the delta winglet-pair ( $b/D=1.08$ )	61

Figure 5.14	Three dimensional particle paths behind the delta winglet pair in common-flow-up configuration ( $b/D=1.67$ )	62
Figure 5.15	Three dimensional particle paths behind the rectangular winglet-pair in common-flow-up configuration ( $b/D=1.67$ )	63
Figure 5.16	Three dimensional particle paths behind the delta winglet-pair in common-flow-up configuration ( $b/D=1.08$ )	64
Figure 5.17	Nusselt number distribution on the bottom plate of a channel with built-in circular tube and delta winglet-pair in common-flow-up configuration	65
Figure 5.18	$\overline{Nu}_s$ for a plane channel, channel with built-in circular-tube and channel with built-in circular-tube and delta winglet pair	66
Figure 5.19	Span-averaged Nusselt number distribution for different Reynolds numbers	67
Figure 5.20	$\overline{Nu}_s$ for two different types of winglet-pair	68
Figure 5.21	$\overline{Nu}_s$ for the delta winglet-pairs with different $b/D$	69
Figure 5.22	Grid independence test	70
Figure 5.23	Comparison between the present computation and experimental results	71

## Nomenclature

B	channel width
b	lateral distance between trailing edges of a winglet-pair
$C_p$	specific heat of the fluid
CV	control volume
D	diameter of the cylinder
F	mass flux through a cell face
H	channel height
k	thermal conductivity of the fluid
$Nu$	local Nusselt number, $\frac{1}{(1-\theta_b)} \left\{ \frac{\partial \theta}{\partial Z} \right\}_{Z=1w}$
$\overline{Nu}$ ,	span averaged Nusselt number, $\int Nu \, dy \, / \, \int dy$
p	static pressure
$Re$	Reynolds number based on channel height $\frac{\rho U_{av} H}{\mu}$
S	surface area of a cell face
t	time
u	axial velocity
v	spanwise velocity
w	normal or vertical velocity
x	axial dimension of coordinates
y	spanwise dimension of coordinates
z	normal or vertical dimension of coordinates
T	temperature

### Greek Letters

$\alpha_1, \alpha_2, \alpha_3$  coefficients of linearly independent unit vectors

$\rho$	density of the fluid
$\theta$	non-dimensional temperature $(T - T_{\infty}) / (T_w - T_{\infty})$

#### Subscripts

b	bulk condition
j	cell face
i	cell center
w	wall

#### Superscripts

$n, \quad n + 1$	time level
------------------	------------



## **Chapter 1**

### **Introduction**

#### **1.1 Motivation**

Fin-tubes are commonly used in gas-liquid crossflow heat exchangers. In such heat exchangers, the gas generally flows across the tubes and the liquid flows inside the tubes. The fins act as extended surfaces providing the bulk of the heat transfer area on the gas side. Even with the extended surfaces, the dominant thermal resistance is on the gas side. In order to achieve significant enhancement of heat transfer on the gas side, strategies must be developed. The heat transfer coefficients on the fin and the outer surfaces of tubes are to be enhanced keeping the pressure penalty within a modest limit.

#### **1.2 The Importance in Technology and Applications**

Heat exchangers are widely used in power and process industries. Improvement in their performance is of great technical, economical, and ecological importance. Existing air-cooled condensers in geothermal power plant use fin-tube heat exchangers with circular tube. The size of heat exchangers is quite large, consuming a large fraction of overall capital cost of these plants. Accomplishment of more efficient heat transfer on the airside of the air-cooled condensers can reduce its size and can improve the overall performance of all the geothermal plants. A modest additional pressure drop across the heat exchangers must support the enhancement of heat transfer. Figure 1.1 shows a schematic diagram of the core region of fin-tube heat exchangers. The protrusions on the flat surfaces can disrupt the growth of thermal boundary layer and increase the transport coefficients. The protrusions in the form of delta wings or winglets can bring about the desired augmentation at the expense of small increase in pressure drop.

### 1.3 Focused Area and Specific Outline of the Present Problem

One of the effective methods of reducing the thermal resistance is induction of longitudinal streamwise vortices in the flow field. The longitudinal vortices interact with an otherwise two-dimensional boundary layer and produce a three-dimensional swirling flow that mixes the near wall fluid with the free stream. Such kinematic mixing strongly enhances the entrainment of fluid from the periphery to the core region of the flow field. As a result, thermal boundary layer is disrupted and heat transfer is enhanced. The longitudinal vortices can be created by mounting delta wing or delta winglet type of vortex generators on the flat surface (Figure 1.2). The longitudinal vortices develop along the side-edges of the delta-winglets due to the pressure difference between the front surface facing the flow and the back surface. These vortices are also called the streamwise vortices since the axes of vortices are aligned to the flow direction. The pressure drop caused due to such vortices is modest because form drag for such winglet-type slender bodies is low. Vortex generators can be mounted behind the tubes in fin-tube heat exchangers in two common configurations – (i) common-flow-down and (ii) common-flow-up as proposed by Pauley and Eaton (1988). In a common-flow-down configuration, the transverse distance between the leading edges of the winglet pair is less than the transverse distance between the trailing edges. On the other hand, in a common-flow-up configuration, the transverse distance between the leading edges of the winglet pair is more than that between the trailing edges.

In order to achieve the objectives enumerated earlier, present investigation has been carried out for the flow and heat transfer in fin-tube cross-flow heat exchangers with delta-winglets mounted behind the tube in common-flow-up arrangement. Numerical investigation on the related topic has been carried out earlier by Biswas et al. (1994). They have used the winglets with common-flow-down arrangement. Torii et al. (2001) have proposed a novel technique of placing the winglets with common-flow-up arrangement. Figure 1.3 presents a sectional view of the suggested arrangement for the fin-tube heat exchangers with delta-winglets placed behind the tube in common-flow-up configuration. For such a

configuration, the full Navier-Stokes equations together with the energy equations are solved and a detailed analysis of flow structure together with heat transfer characteristics is carried out

## **1.4 Layout of the Thesis**

In Chapter-1 we have already introduced the genesis of the problem. Chapter-2 of the thesis provides a review of the literature relevant to the understanding of the basic mechanism involved in augmentation of heat transfer and the algorithms related to solving the Navier-Stokes equations. The mathematical formulation of the problem is presented in Chapter-3. Here, the geometry of interest, the governing equations, boundary conditions are discussed. Chapter-4 discusses the grid generation technique, the solution algorithm and the mathematical foundation of the finite volume formulation in detail. Chapter-5 discusses the results of the present investigation with emphasis on flow physics and associated heat transfer. Chapter-6 includes the concluding remarks and the scope for the future research.

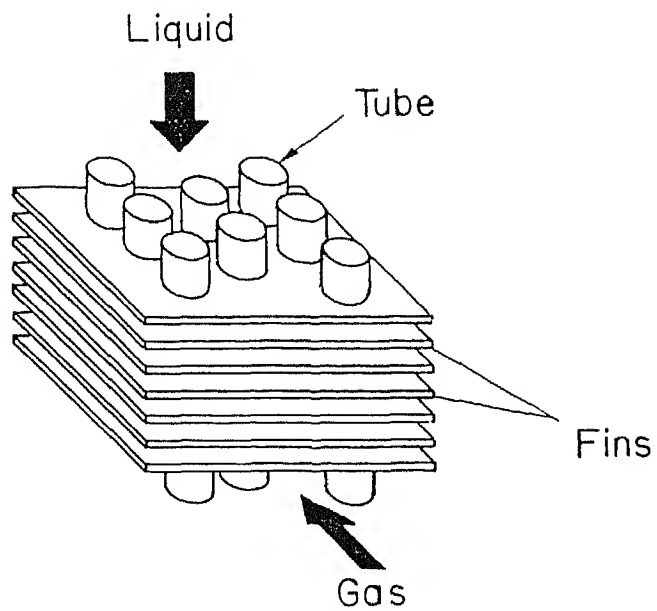


Figure 1.1 Schematic diagram of core region of a fin-tube heat exchanger

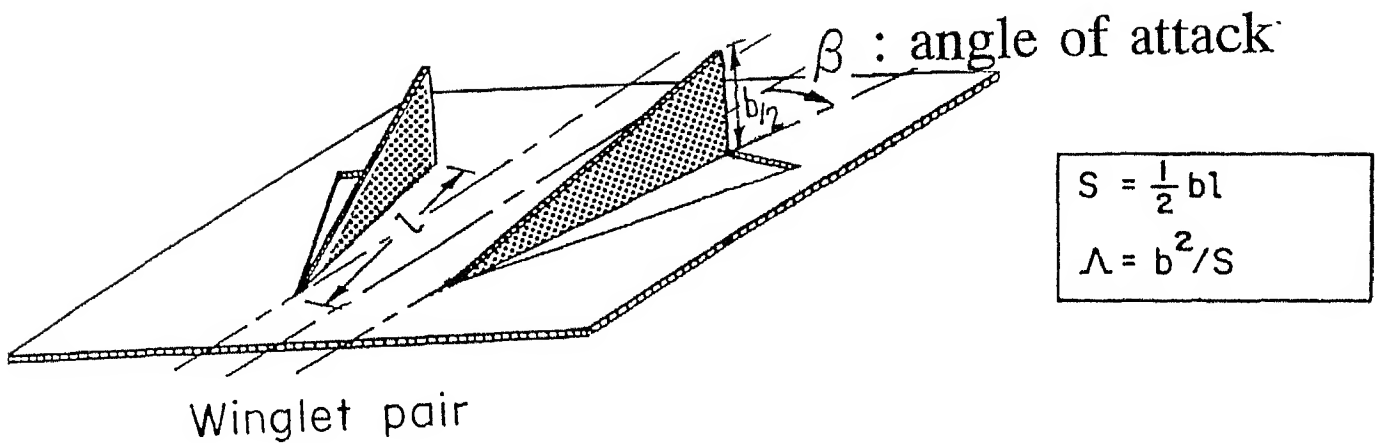


Figure 1.2 Delta-Winglet type vortex generators on flat surface

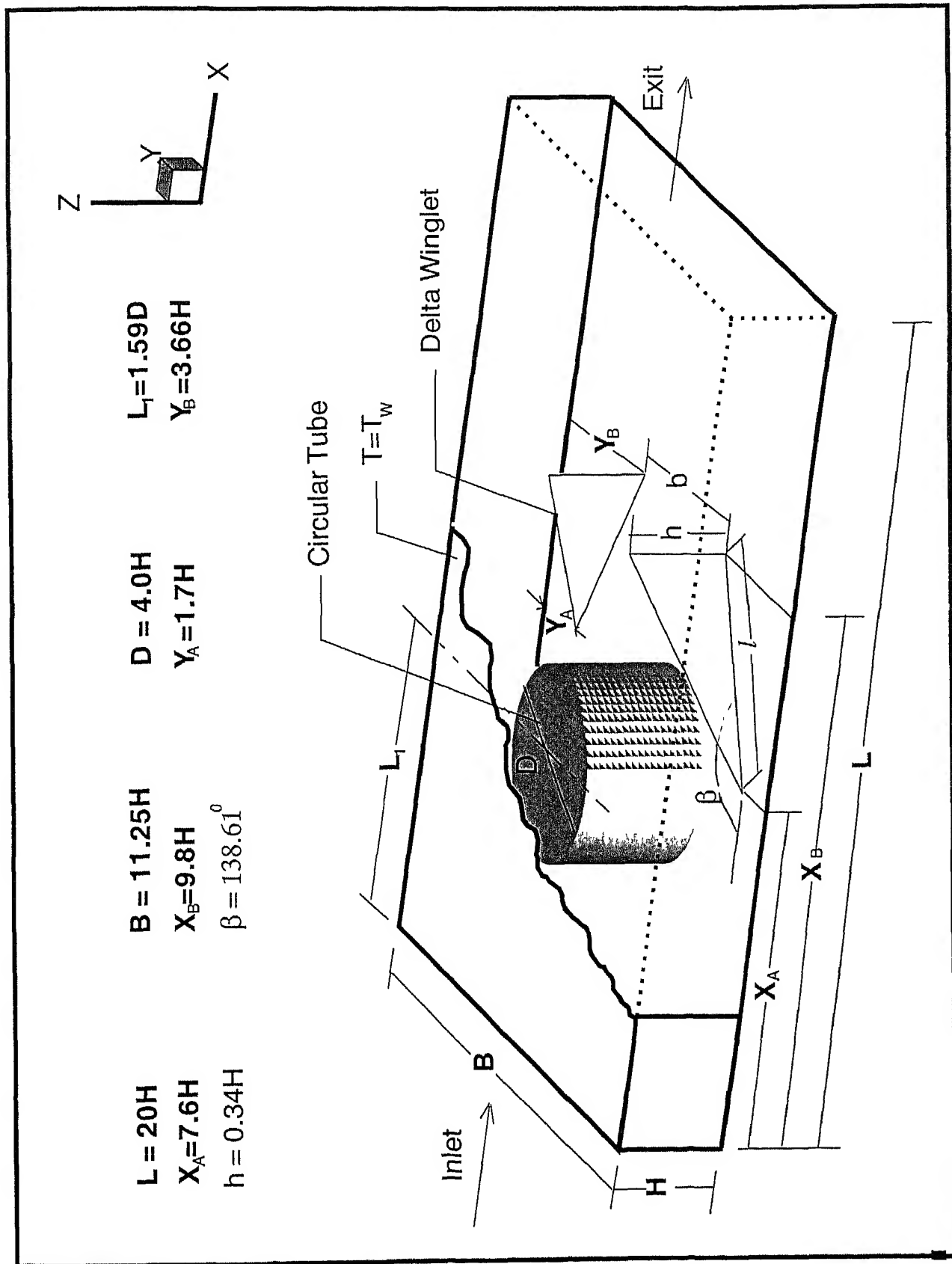


Figure 1.3 Heat exchanger module considered in present investigation

## Chapter 2

### Literature Survey

#### 2.1 Introduction

This chapter is divided in three different sections. The first section provides an overview of work done by various researchers in the area of enhancement of heat transfer. Quite appreciable amount of experimental and computational research have been carried out in the area of heat transfer augmentation. Especially concerned literature on enhancement through manipulation of surface geometry, which has been analyzed by many researchers, is presented in this chapter. The next section focuses on the work done in the field of incompressible flow modeling and associated heat transfer problems. The third section discusses aspects of unsteady flow and turbulence. Finally the benefit of current problem is established from the existing literature.

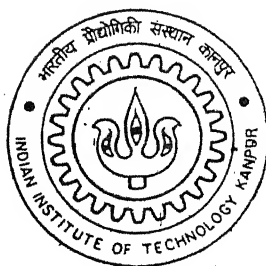
#### 2.2 Augmentation of Heat transfer

The present aim of the study is to enhance the heat transfer on the gas side of the fin-tube heat exchangers and to minimize the space occupied by the equipment for a desired rate of heat transfer. With this intent we would like to study different investigations related to the augmentation of heat transfer suitable for the applications mentioned above.

The representative element of a fin-tube heat exchanger consists of a rectangular channel with built-in circular tube (Figure 2.1). In channel flows, rate of heat transfer between fluid and channel walls deteriorates as boundary layer grows on the channel walls and flow tends to become fully developed. Protrusions can be mounted on this channel walls in order to disrupts the growth of boundary layers and thereby enhance the heat transfer between the flowing fluid and channel wall. To achieve this goal, protrusions in form of slender delta wings or winglets can be mounted . The longitudinal vortices are generated along the side edge of the wing shaped vortex generators due to pressure difference between the front surface

# **WINGLET-TYPE VORTEX GENERATORS WITH COMMON-FLOW-UP CONFIGURATION FOR FIN-TUBE HEAT EXCHANGERS**

By  
**ASEEM JAIN**



DEPARTMENT OF MECHANICAL ENGINEERING  
**Indian Institute of Technology Kanpur**  
NOVEMBER, 2001

facing the flow and the back surface. Investigations on the enhancement of heat transfer by vortex generators have been carried out in the last two decades by Fiebig et al. (1986), Turk and Junklan (1986), Eibeck and Eaton (1987), Fiebig et al. (1989), Tiggelbeck (1994), Yanagihara and Torii (1990), Fiebig et al. (1990), Fiebig et al (1991), Sanchez (1989), Biswas et al (1994) and Valencia (1996). The idea of using vortex generators in compact heat exchangers has already been implemented by industry. Fiebig and his co-workers (Fiebig et al. 1986) experimentally observed enhancement in heat transfer using vortex generators on the primary heat transfer surfaces. Subsequently a host of other investigations were taken up by different groups and the use of vortex generators evolved as a device for enhancement in heat transfer. Biswas and Chattopadhyay (1992) have considered the influence of Reynolds number and angle of attack on skin friction and Nusselt number for delta wing type vortex generators in a channel.

Fiebig and his co-workers (1991) conducted an experimental study to compare the performance of delta wings, delta winglets, rectangular wings and rectangular winglets as the enhancement device. Delta wings and winglets were found to be more effective than rectangular wing and winglets. For the simple case of a flat plate with a delta wing attached to its leading edge, Gentry and Jacobi (1997) presented a method for selecting the preferred wing aspect ratio and attack angle. The interaction of vortices with the boundary layer and its effect on heat transfer is a subject of interest to many researchers. Some notable investigations include Taylor-Gortler vortices in boundary layers on concave surfaces, the horseshoe vortices formed by an obstruction protruding from the inner surface and wingtip vortices impinging on a downstream surface. The embedded vortex is capable of strongly perturbing the boundary layer and influencing the heat transfer characteristics. In addition, longitudinal vortices usually maintain their coherence over a long streamwise distance. As a consequence, the heat transfer effects behind the vortex generators are very persistent. Eibeck and Eaton (1987), Westpal and Mehta (1987) have worked extensively in this field with more focus to the turbulent boundary layers. Eibeck and Eaton (1987) have conducted experiments on longitudinal vortices embedded in a turbulent boundary layer and



resultant heat transfer effects. Longitudinal vortices are found to influence the heat transfer behavior significantly. Local Stanton number increase is as high as 24 percent resulting in a net increase in spanwise average heat transfer coefficient.

### **2.3 Literature on Incompressible Flow Modeling and Associated Heat Transfer Problems**

During past three decades various numerical techniques for modeling incompressible flows have been developed. Such techniques involve numerical solution of full Navier-Stokes equations and energy equations for obtaining the temperature field. The major difficulty encountered during the solution of incompressible flows arises from the absence of any explicit equation for pressure and due to the nature of spatial coupling of the pressure and velocity. For incompressible flow problems, pressure does not have its usual thermodynamically meaning. Here it is a relative variable, which adjusts itself instantaneously for the condition of zero mass divergence to be satisfied at all computational cells. This behavior is reflected from the fact that in an incompressible fluid speed of sound is infinite. As a consequence, the pressure field cannot be solved by explicit time advancement procedure, instead it requires at least a partially implicit determination which takes into account the coupling between pressure and velocity fields as well as the effects of velocity boundary conditions. This aspect is the most distinctive feature of the primitive variable formulation of the incompressible flow modeling. The difficulty of determination of pressure field can be resolved in the stream function-vorticity approach. But this approach loses its attractiveness when three-dimensional flow is computed because of absence of a single scalar stream function in the three-dimensional space. Efforts has been made so that two as well as three-dimensional problems could be computed following a primitive variable approach without encountering non-physical wiggles in pressure distribution. As a remedy, it has been suggested to employ a different grid for each variable. Harlow and Welch (1965) have used a staggered grid for the dependent variables in their well-known MAC (Marker and Cell) method. The MAC method of Harlow and Welch is one of the earliest

and widely used explicit methods for solving the full Navier-Stokes equations. The MAC method uses a layer of imaginary cells around the boundary of the physical domain necessitating the updating of the boundary conditions after every change in the internal velocity and pressure values. The original version of MAC method has been modified by Harlow and Amsden, popularly known as Simplified MAC (SMAC, 1970). Nicholas and Hirt (1971) and Hirt and Cook (1972) have also used a modified version of MAC algorithm for application of free surface flows. The MAC method has been successfully used by many researchers to simulate even highly unsteady and turbulent flows (Robichaux, Tafti and Vanka, 1992). It has been experienced that the MAC method is indeed very efficient in the study of temporal flow development. It has stability restrictions on the time increment, which slows down the calculation for steady flow considerably. Since implicit methods have no such restrictions, they are more attractive.

Mukhopadhyay et al. (1993) have developed a numerical method for predicting viscous flows for incompressible geometries. Integral mass and momentum conservation equations are deployed and these are discretized into algebraic form through numerical quadrature. The physical domain is divided into a number of non-orthogonal control volumes that are isoparametrically mapped onto standard rectangular cells. Verma and Eswaran (1996) and Verma and Eswaran (1997) have developed a finite volume based flow solver for complex geometries using overlapping control volumes.

Patankar and Spalding (1972) have introduced an efficient method known as SIMPLE (Semi-Implicit Method for Pressure Linked Equations). This method is based on finite volume discretization of the governing equations on a staggered grid. In order to improve the convergence involved in the solution of pressure equation, several variants of SIMPLE algorithm have been developed. The SIMPLER algorithm of Patankar (1981) and SIMPLEC algorithm of Van Doormaal and Raithby (1984) are improvements on SIMPLE. Although changes to incorporate SIMPLEC into SIMPLE algorithm are minor, the consequences can be great as it eliminates the approximations made in SIMPLE while deriving

the equation for pressure-velocity correction. Garg and Maji (1987) have applied SIMPLEC (Van Doormaal and Raithby, 1984) method for solution of viscous flows through periodically converging-diverging tubes. Application of finite volume methods using non-orthogonal coordinates and collocated grid arrangement is reported by Rhie and Chow (1983) and Peric (1985). Peric et al. (1988) have shown that collocated arrangement converges faster than the staggered variable arrangement and has advantages when extensions such as multigrid techniques and non-orthogonal grids are considered. An appropriate pressure interpolation avoids the pressure splits in collocated grid arrangement. A finite volume based procedure with momentum interpolation has been successfully developed by Majumdar (1988) using such collocated velocities and pressure. Kobayashi and Pereira (1991) have modified the momentum interpolation method suggested by Peric (1985) and named it as Pressure-Weighted Interpolation Method Corrected (PWIMC). In this method the non-orthogonal terms in the momentum equations were solved explicitly, whereas in the pressure corrections they were dropped.

It is clear that substantial progress has been made for the development of algorithms for complex incompressible flow simulations but none of the prescriptions is universal. Depending upon the nature of flow and geometry etc., one can always go for the best-suited discretization procedure for solving time-dependent three-dimensional Navier-Stokes equations.

## **2.4 Unsteady flows and Turbulence**

In the experimental investigation of transport process, Cantewell and Coles (1983) have studied the near-wake of a circular cylinder at a very high Reynolds number. The periodic and random components have been shown to have comparable amplitudes. A considerable emphasis has been placed on the topology of the unsteady mean flow. This emerges as a pattern of centers and saddles in a frame of reference moving with the eddies. The kinematics of the vortex formation process has been described through the critical point theory. The important conclusion of the work is that the turbulence production is concentrated

near the saddles. Entrainment of the fluid into the wake is also found to be closely associated with the formation and location of the saddles.

The wake behind circular tube shows unsteady characteristics even at low Reynolds numbers. Reynolds number behaves as control parameter in a dynamical system and as it is increased, detachment of the free shear layer and the consequent shedding of vortices, generation of harmonics, three-dimensionality in nominally two-dimensional geometries, onset of chaos and transition to turbulence results. This by itself is a sequence of transitions, each being identified with a critical Reynolds number and an associated flow topology. A non-linear dynamical system can go to a chaotic state through three distinct routes. These involve period doubling of frequencies (Feigenbaum, 1980), the Ruelle-Takens-Newhouse route through quasi-periodicity (Ruelle and Takens, 1971) and intermittency (Manneville and Pomeau, 1980). Vittori and Blondeaux (1993) have reported a quasi-periodic route to chaos in their numerical study of two-dimensional oscillatory flow around a circular tube. They found that the system gets phase-locked before it becomes chaotic. In the quasi-periodic route, the dynamical system initially at a steady state, becomes unsteady as the control parameter crosses a particular threshold limit. The nonlinearity of the system generally increases as a result of an increase in control parameter. For example, an increase in the Reynolds number diminishes diffusion and dissipation mechanisms, resulting in greater prominence of the non-linear acceleration terms. As a consequence of instability, the dynamical behavior approaches a limit cycle caused by a Hopf bifurcation. Similarly, further increase of Reynolds number leads to appearance of three frequencies. Guzman and Amon (1996) have shown a quasi-periodic and frequency locking route to chaos in two as well as three-dimensional converging-divergence channels. They have found that the flow undergoes a rapid transition to a chaotic three-dimensional state at a Reynolds number of 500 starting from a laminar two-dimensional state at a Reynolds number of 200. In the work of Pulliam and Vastano (1993), the transition to chaos of an open unforced two-dimensional flow past an aerofoil has been documented. The salient findings of their study are that the system undergoes period-doubling

bifurcations to chaos as the Reynolds number is increased from 800 to 1600. The dominant harmonics present in the signal can be identified with the help of FFT (Fast Fourier Transformation) of the time series data.

## **2.5 How the Current Problem Benefits from Existing Literature**

The numerical investigations of Biswas et al. (1994) and the experimental findings of Valencia et al. (1996) reveal the effective utilization of vortex generators for the purpose of enhancement of heat transfer while producing less of a pressure drop. In the above investigations, the enhancement of heat transfer from the fin surfaces is achieved by placing delta-winglet type vortex generators on the flat fin surfaces in the neighborhood of the tube. In the related study of Tsai et al. (1999), the use of wavy-type extended fin surfaces as device for enhancement of heat transfer in the fin-tube heat exchangers has been deployed. The longitudinal vortices or streamwise vortices get developed along the side edges of the delta-winglets due to pressure difference between the front surface and the back surface. These vortices interact with the boundary layer and produce a three-dimensional swirling flow that mixes near wall fluid with the free-stream. The mechanism strongly enhances the entrainment of fluid from the periphery to the core region of the flow field. Thus the thermal boundary layer is disrupted and the local heat transfer rate is enhanced. The additional pressure losses are modest because the form drag for such winglet-type slender bodies is low.

The air-cooled condensers of geothermal plants consist of the same fin-tube arrangement as shown in Figure 2.1. Air is forced through several rows of these fin-tubes by large fans. The condensers units can be very large, consuming a large fraction of the overall capital cost of these plants. In the present research, a three-dimensional numerical model has been formulated to provide a better insight into the flow physics. The complete Navier-Stokes equations together with governing equations of energy are solved in an element of heat exchanger as shown in Figure 1.3. The heat exchanger element consists of a rectangular channel with a built-in circular tube and a winglet pair. A detailed analysis of the flow structure

along with heat transfer characteristics in such an element is studied in this investigation. In general, the delta-winglet type vortex generators can be mounted on the flat surfaces with common-flow-down configuration. For such a configuration, the transverse distance between the leading edges of the winglet pair is less than the transverse distance between the trailing edges of the winglet pair (Pauley and Eaton, 1988). In the present case of common-flow-up configuration, transverse distance between the leading edges of the winglet pair is more than that between the trailing edges. Torii et al. (2000) have indicated that the delta winglet pair with common-flow-up configuration creates constricted passages in the aft region of the tube, which brings about separation delay. The fluid is accelerated in the constricted passages, and as a consequence, the point of separation travels downstream. Narrowing of the wake and suppression of vortex shedding are the obvious outcome of such configurations. Since the fluid is accelerated in this passage, the zone of poor heat transfer is also removed. The poor heat transfer zone is created in the wake of the tube in absence of any vortex generators. The common-flow-up configuration of the delta winglet pair emerges as the most attractive enhancement technique for the air-cooled condensers.

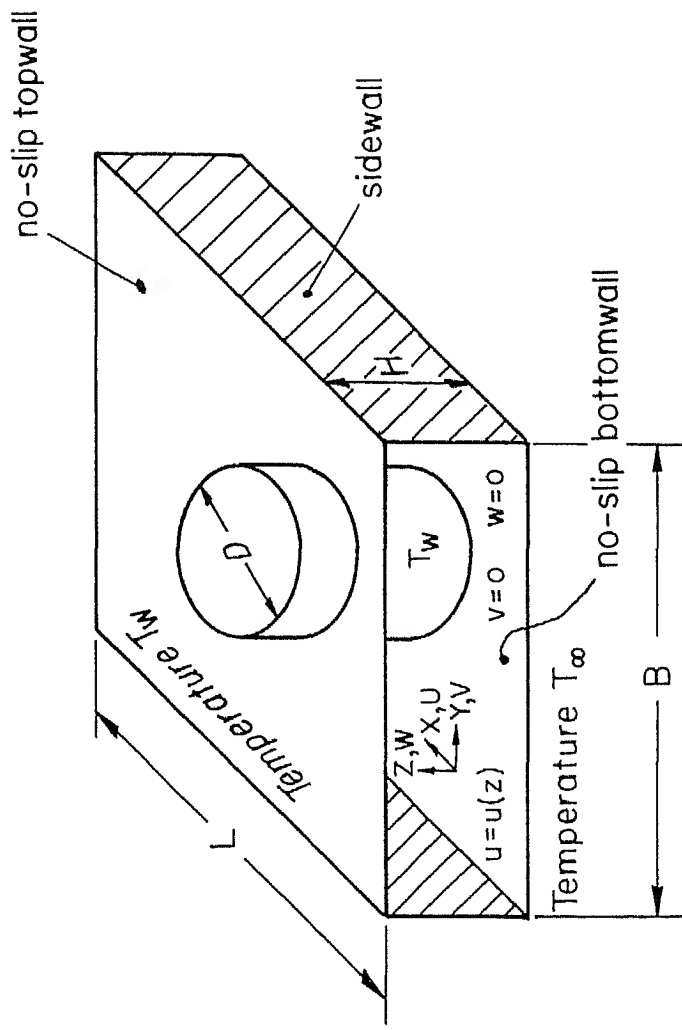


Figure 2.1 Element of existing fin-tube heat exchanger

## Chapter 3

### Mathematical Formulation

#### 3.1 Introduction

Arising out of practical importance of enhancement of heat transfer in fin-tube heat exchangers a need is felt to analyze the flow field in a representative element of the heat exchanger. The computation involves determination of flow and heat transfer characteristics in a horizontal channel with a built-in circular tube and a pair of winglets. The numerical simulation can provide point by point information of flow structure and temperature distribution in an element of a fin-tube heat exchanger along with the effect of various parameters on heat transfer enhancement.

#### 3.2 Statement of the Problem

Figure 1.3 represents the computational domain. Two neighboring fins form a channel of height  $H$ , width  $B = 11.25H$  and length  $L = 20H$ . The circular tube of diameter  $D = 4.0H$  is located at a distance  $L_1 = 1.59D$  from the inlet. The blockage ratio,  $D/B$  has been kept 0.36. The position of the winglet is given by  $X_A = 7.6H$ ,  $X_B = 9.8H$ ,  $Y_A = 1.7H$ , and  $Y_B = 3.66H$ . The height of the winglet,  $h = 0.347H$  and the angle of attack,  $\beta = 138.61^\circ$ . Air has been used as the working fluid; hence the Prandtl number of this study is 0.7.

The flow field in the channel with built-in circular tube and a winglet pair is characterized by the following parameters

- Reynolds Number
- Position of the oval tube in the channel ( $L_1/L$ )
- Velocity profile at the channel inlet
- Channel height ( $H/B$ )



- Angle of attack of the winglets ( $\beta$ )
- Height of the winglets ( $h/H$ )
- Position of the winglets ( $X_A/L, Y_A/L$ )

### 3.3 Governing Equations

The three-dimensional Navier-Stokes equations for laminar flow of an arbitrary spatial control volume  $V$  bounded by a closed surface  $S$  can be expressed in the following general convection-diffusion-source integral form

$$\frac{\partial}{\partial t} \int_V \rho dV + \int_S \rho \mathbf{u} \cdot d\mathbf{S} = 0 \quad (3.1)$$

$$\frac{\partial}{\partial t} \int_V \rho \phi dV + \int_S [\rho \mathbf{u} \phi - \Gamma_\phi \nabla \phi] \cdot d\mathbf{S} = \int_V S_\phi dV \quad (3.2)$$

Where  $\rho$  represents the fluid density,  $\mathbf{u}$  is the fluid velocity,  $\phi$  stands for any vector component or scalar quantity,  $S_\phi$  is the volumetric source term. For incompressible flow of Newtonian fluid, the equation takes the form

$$\int_S \mathbf{u} \cdot d\mathbf{S} = 0 \quad (3.3)$$

$$\frac{\partial}{\partial t} \int_V \rho \phi dV + \int_S [\rho \mathbf{u} \phi - \Gamma_\phi \nabla \phi] \cdot d\mathbf{S} = \int_V S_\phi dV \quad (3.4)$$

and the source term for momentum equation becomes  $-\frac{1}{\rho} \int_S p \mathbf{I} \cdot d\mathbf{S}$  where  $\mathbf{I}$  is the unit tensor. In this formulation we work with Cartesian components of velocity. So  $\phi$  can be the three-cartesian components of velocity  $u, v, w$  as well as any scalar e.g., temperature which need to be determined. The variables of the general transport equation are given in Table-3.1.

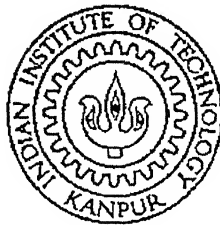
**WINGLET-TYPE VORTEX GENERATORS WITH  
COMMON-FLOW-UP CONFIGURATION FOR  
FIN-TUBE HEAT EXCHANGERS**

*A thesis submitted  
in partial fulfillment of the requirements  
for the degree of*

**MASTER OF TECHNOLOGY**

*by*

**ASEEM JAIN**



**DEPARTMENT OF MECHANICAL ENGINEERING  
INDIAN INSTITUTE OF TECHNOLOGY, KANPUR**

**November, 2001**

Table 3.1: Values of the variables in the general transport Equation (3.2)

Equation	$\phi$	$\Gamma_\phi$	$S_\phi$
Continuity	1	0	0
Momentum	$U_j$	$\mu$	$\frac{\partial p}{\partial x_j}$
Energy	T	$\frac{k}{C_p}$	0

### 3.4 Boundary Conditions

The governing differential equations are elliptic in space and parabolic in time. We need the boundary conditions for all the confining surfaces. The boundary conditions of interest in the present investigation are:

Top and bottom plates

$$u=v=w=0, \quad (\text{No Slip boundary condition}) \text{ and } \frac{\partial p}{\partial z} = 0$$

$$T = T_w \quad (T_w \text{ represents wall temperature})$$

Side Wall

$$\frac{\partial u}{\partial y} = \frac{\partial w}{\partial y} = 0, \quad v = 0 \quad (\text{Free Slip boundary condition}) \text{ and } \frac{\partial p}{\partial y} = 0$$

$$\frac{\partial T}{\partial y} = 0$$

Channel Inlet

$$u = u_\infty, \quad v=w=0, \quad \text{and} \quad \frac{\partial p}{\partial x} = 0$$

$$T = T_\infty$$

Channel Exit

The mass flux through the outlet boundaries is found by means of a continuative outflow condition (Orlanski (1976)), which allows changes inside the flow field to be transmitted outward, but not vice-versa.

$$\frac{\partial \phi}{\partial t} + U_{av} \frac{\partial \phi}{\partial x} = 0 \quad (\text{Where } \phi \text{ represents } u, v, w \text{ or } T)$$

$$p = p_{\infty}$$

Obstacles: Circular tube and the Winglet pair

$$u=v=w=0, \text{ and } \frac{\partial p}{\partial n} = 0 \quad (\text{where } n \text{ signifies normal direction})$$

$$\text{and } T = T_w$$

## Chapter 4

### Grid Generation And Method Of Solution

#### 4.1 Introduction

In order to solve numerically the governing equations in the prescribed computational domain with given initial and boundary conditions, two major discretization steps have to be performed. First being the discretization of domain, numerical grid is generated for computation. Second is the discretization of the governing equations. Various methods of discretization can be used for a given set of partial differential equations. The most common methods used are finite differences, finite volumes and finite elements. In present computation, a finite volume scheme has been used for spatial discretization of governing equations. Conservative formulation of discretization is followed, assuring automatically the satisfaction of the global balance of the conserved quantities, independent of the coarseness of the numerical grid.

#### 4.2 Grid Generation

Figure 4.1 shows the schematic three-dimensional grid for the computation. A differential equation is used to generate the body fitting type two-dimensional grid where circular tube and a pair of winglets are placed. The two dimensional grid is stacked layer by layer in third direction to generate the grid in that direction.

Initially two-dimensional grid is generated by the transfinite interpolation, which uses essentially linear interpolation scheme to compute the interior points by using the points from the computational domain boundaries. Thus an algebraic grid is obtained, which is further smoothened by the use of Partial Differential Equations (PDE). In this technique, a system of elliptical PDEs is solved for

obtaining the location of grid points in the physical space, whereas on the computational space, transformed grid is of rectangular shape with uniform spacing. A Laplace equation or a Poisson equation with a Dirichlet boundary condition can be used for this purpose. Standard Poisson equation is of the form

$$\begin{aligned}\nabla^2 \xi &= P \\ \nabla^2 \eta &= Q\end{aligned}\tag{4.1}$$

Where P and Q are known as control functions. Here we use Laplace equation in the following way

$$\begin{aligned}\nabla^2 \xi &= 0 \\ \nabla^2 \eta &= 0\end{aligned}\tag{4.2}$$

The above equations can be solved by finite difference technique to get the location of the interior points from the boundary values. The algebraic mapping can generate initial guess, needed to solve the Laplace equation. The Laplacian operator can provide quite smooth grids. The grid lines generated remain equally spaced if boundary curvature is absent but show a tendency to concentrate near curved boundaries. By using the appropriate control functions in the Poisson Equation, this drawback can be removed. But the use of control functions add more complexity in the transformed domain.

### 4.3 Computational Procedure for Grid Generation

The algorithm used for the generation of the present grid can be outlined as follows:

1. Geometrical data is used as input.
2. The computational grid is defined on  $\xi$ - $\eta$  plane based on the number of grid points.
3. Boundary points along the edges of the physical domain are defined.
4. Algebraic grid is used to generate the initial guess by using liner interpolation technique, which is used by the Laplacian operator.
5. Using four-point formula, guess is further improved a little.

6. Elliptic grid generation system constitutes of following equations derived from the Laplace operator

$$\alpha x_{\xi\xi} - 2\beta x_{\xi\eta} + \lambda x_{\eta\eta} = 0 \quad (4.3)$$

$$\alpha y_{\xi\xi} - 2\beta y_{\xi\eta} + \lambda y_{\eta\eta} = 0$$

Where

$$\alpha = x_{\eta}^2 + y_{\eta}^2$$

$$\beta = x_{\xi} x_{\eta} + y_{\xi} y_{\eta}$$

$$\lambda = x_{\xi}^2 + y_{\xi}^2$$

Here subscripts indicate partial derivatives of Cartesian variables with respect to curvilinear variables.

These coefficients are determined using finite difference approximations. Their values in these expressions are provided by the initial distributions for the first iteration, and subsequently from the previous iteration, i.e., the computation of coefficients lag by one iteration level. The iterative solution continues until a specified convergence criterion is met.

Because of discretized approximation of differential equations, the truncation error in numerical analysis is much dependent on the nature of grid. We target for a grid, which gives minimum truncation error.

The Parameters that affect the quality of the grid are:

1. Transformation Jacobian
2. Skewness
3. Aspect Ratio
4. Adjacent cell ratio

A desirable grid should have nonzero transformation Jacobian almost at each location of the grid cells. It should be of similar order of magnitude with no quite small values appearing anywhere. It should possess least possible skewness, aspect ratio close to 6 and adjacent cell ratio close to one.

#### 4.4 Finite Volume Method

The conservation equations are discretized employing the finite-volume approach of Eswaran and Prakash (1998). The solution domain is divided into a number of contiguous (finite) control volumes (CV). The coordinates of the control volume vertices are calculated by the grid generation procedure. These vertices, which are assumed to be connected by straight lines, define the control volume. A **collocated grid** arrangement is employed and all the dependent variables ( $u$ ,  $v$ ,  $w$ ,  $p$ ,  $T$ ) are defined at the same location, the centroid of the control volume (Figure 4.2). Cartesian velocity components have been used. The symbols, E, W, N, S, T and B indicate the six neighboring control volume centers for the east, west, north, south, top and bottom neighbors. The face center points  $e$ ,  $w$ ,  $n$ ,  $s$ ,  $t$  and  $b$  are located at the intersection of the lines joining the midpoints of the opposite edges. Edge centers  $te$ ,  $be$ ,  $ne$  and  $se$  are the midpoints of the edges that form the east face with  $e$  as the center of the cell face. Similarly  $tw$ ,  $bw$ ,  $nw$ ,  $sw$ ,  $tn$ ,  $bn$ ,  $ts$  &  $bs$  are located at the corresponding center of edges that form west, north & south face.

The advantages of the collocated grid over staggered grids, especially when the non-orthogonal coordinates are:

- There is only one set of control volume as all the variables share the same location.
- The convection contribution to the coefficients in the discretized equations is same for all variables.
- When coordinate oriented velocity components are used, it results in simpler equations.
- Number of constraints on the numerical grid is reduced.



## 4.5 Surfaces areas and Volumes

Figure 4.2 shows the corner points of the control volume numbered as 1,2,3, etc. The outward surface normal and volume can be found in the following manner as suggested by Kordulla and Vinokur (1983).

Defining  $\mathbf{r}_{ij} = \mathbf{r}_i - \mathbf{r}_j$  where  $\mathbf{r}_i$  and  $\mathbf{r}_j$  indicate the position vectors of points  $i$  and  $j$  respectively, we have the formulate the expressions for calculating the surface area and volume for different faces.

- East Face 
$$\mathbf{S}_e = \frac{1}{2} (\mathbf{r}_{74} \times \mathbf{r}_{83}) \quad (4.4)$$

- West Face 
$$\mathbf{S}_w = \frac{1}{2} (\mathbf{r}_{16} \times \mathbf{r}_{52}) \quad (4.5)$$

- North Face 
$$\mathbf{S}_n = \frac{1}{2} (\mathbf{r}_{27} \times \mathbf{r}_{63}) \quad (4.6)$$

- South Face 
$$\mathbf{S}_s = \frac{1}{2} (\mathbf{r}_{18} \times \mathbf{r}_{45}) \quad (4.7)$$

- Top face 
$$\mathbf{S}_t = \frac{1}{2} (\mathbf{r}_{75} \times \mathbf{r}_{68}) \quad (4.8)$$

- Bottom Face 
$$\mathbf{S}_b = \frac{1}{2} (\mathbf{r}_{13} \times \mathbf{r}_{24}) \quad (4.9)$$

The volume of the cell is calculated from the cell coordinates, with the assumption that the linear segments to form the six cell faces join the cell corners. The volume is calculated as follows

$$V = \frac{1}{3} \mathbf{r}_{71} \cdot (\mathbf{S}_s + \mathbf{S}_b + \mathbf{S}_w) \quad (4.10)$$

## 4.6 Discretization Procedure

The main steps for the discretization of the integral governing equations involve the calculation of convection and the diffusion fluxes and source terms. The rates of change and source terms are integrated over the cell volume, whereas the

convection and the diffusion terms form the sum of fluxes through the faces of the control volume.

#### 4.6.1 Discretization of Continuity Equation

Equation 3.1 is discretized in the following manner:

$$\int_S \rho \mathbf{u} \cdot d\mathbf{S} \approx \sum_{j=e,w,n,s,t,b} \rho (\mathbf{u} \cdot \mathbf{S})_j = \sum_j \rho \mathbf{u}_j \cdot \mathbf{S}_j \quad (4.11)$$

Where  $\mathbf{S}_j$  is the surface vector representing the area of the  $j^{\text{th}}$  cell face and  $\mathbf{u}_j$  is the velocity defined at the face center  $j$ .

In discretized form continuity equation becomes

$$\sum_j F_j = F_e + F_w + F_n + F_s + F_t + F_b = 0 \quad (4.12)$$

where the  $F_j$  is the outward mass-flux through face  $j$ , defined by:

$$F_j = \rho \mathbf{u}_j \cdot \mathbf{S}_j$$

#### 4.6.2 Discretization of General Equation

##### (a) Rate of Change

The value of dependent variable  $\phi$  at the centroid of the control volume represents an average over the CV as a whole. Thus

$$\frac{\partial}{\partial t} \int_V \rho \phi dV \approx \frac{(\rho \phi V)_P^{n+1} - (\rho \phi V)_P^n}{\Delta t} \approx \rho V \frac{\phi_P^{n+1} - \phi_P^n}{\Delta t} \quad (4.13)$$

Where  $V$  is the volume of the cell.

(b) **Convection Fluxes**

The surface integral over convection flux of variable  $\phi$  can be approximated in the following form

$$\int_S \rho \mathbf{u} \phi \cdot d\mathbf{S} \approx \sum_j \rho \phi_j (\mathbf{u} \cdot \mathbf{S})_j = \sum_j F_j \phi_j \quad (4.14)$$

Where  $\phi_j$  is the value of  $\phi$  at the center of face j. Thus

$$\int_S \rho \mathbf{u} \phi \cdot d\mathbf{S} \approx F_e \phi_e + F_w \phi_w + F_n \phi_n + F_s \phi_s + F_t \phi_t + F_b \phi_b \quad (4.15)$$

Where,  $\phi_e$  is the (interpolated) value of the variable  $\phi$  at the east face center, etc. This can be evaluated by using a central difference linear interpolation between the neighboring nodal values  $\phi_P$  and  $\phi_E$ . At east face the value of  $\phi_e$  is given by

$$\phi_e = \frac{V_E}{V_E + V_P} \phi_P + \frac{V_P}{V_E + V_P} \phi_E \quad (4.16)$$

Where  $V_E$  and  $V_P$  are volumes of the cells around the points E and P respectively and  $\phi_E$  and  $\phi_P$  are the values of the dependent variables at these points. In a collocated grid system, all dependent variables are defined at the same location hence exactly the same interpolation scheme is used to express all of them at the interfaces. The central difference approximation to compute the convection flux may lead to numerical stability therefore it is blended with first order upwind differencing scheme (UDS) as follows

$$F_e \phi_e = (F_e \phi_e)^{\text{CDS}} + \gamma [ (F_e \phi_e)^{\text{UDS}} - (F_e \phi_e)^{\text{CDS}} ] \quad (4.17)$$

The upwind differencing scheme is based on assumption that the convected flux at cell face is equal to that at upstream cell along the same coordinate direction.

Thus the value  $\phi_e$  at east face is assigned the value  $\phi_P$  if  $u_e \geq 0$ . This can be conveniently summarized as

$$F_e \phi_e = F_e \left( \frac{V_E}{V_E + V_P} \phi_P + \frac{V_P}{V_E + V_P} \phi_E \right) + \gamma \left\{ \phi_P [ [F_e, 0] ] - \phi_E [ [-F_e, 0] ] - F_e \left( \frac{V_E}{V_E + V_P} \phi_P + \frac{V_P}{V_E + V_P} \phi_E \right) \right\} \quad (4.18)$$

The symbol  $[ [ , ] ]$  signifies greatest of the two quantities inside the brackets and  $\gamma$  is upwind factor. Similar expressions can be written for the other cell faces (Eswaran et al. 1998).

$$F_w \phi_w = F_w \left( \frac{V_W}{V_W + V_P} \phi_P + \frac{V_P}{V_W + V_P} \phi_W \right) + \gamma \left\{ \phi_P [ [F_w, 0] ] - \phi_W [ [-F_w, 0] ] - F_w \left( \frac{V_W}{V_W + V_P} \phi_P + \frac{V_P}{V_W + V_P} \phi_W \right) \right\} \quad (4.19)$$

$$F_n \phi_n = F_n \left( \frac{V_N}{V_N + V_P} \phi_P + \frac{V_P}{V_N + V_P} \phi_N \right) + \gamma \left\{ \phi_P [ [F_n, 0] ] - \phi_N [ [-F_n, 0] ] - F_n \left( \frac{V_N}{V_N + V_P} \phi_P + \frac{V_P}{V_N + V_P} \phi_N \right) \right\} \quad (4.20)$$

$$F_s \phi_s = F_s \left( \frac{V_S}{V_S + V_P} \phi_P + \frac{V_P}{V_S + V_P} \phi_S \right) + \gamma \left\{ \phi_P [ [F_s, 0] ] - \phi_S [ [-F_s, 0] ] - F_s \left( \frac{V_S}{V_S + V_P} \phi_P + \frac{V_P}{V_S + V_P} \phi_S \right) \right\} \quad (4.21)$$

$$F_t \phi_t = F_t \left( \frac{V_T}{V_T + V_P} \phi_P + \frac{V_P}{V_T + V_P} \phi_T \right) + \gamma \left\{ \phi_P [ [F_t, 0] ] - \phi_T [ [-F_t, 0] ] - F_t \left( \frac{V_T}{V_T + V_P} \phi_P + \frac{V_P}{V_T + V_P} \phi_T \right) \right\} \quad (4.22)$$

$$F_b \phi_b = F_b \left( \frac{V_B}{V_B + V_P} \phi_P + \frac{V_P}{V_B + V_P} \phi_B \right) + \gamma \left\{ \phi_P [ [F_b, 0] ] - \phi_B [ [-F_b, 0] ] - F_b \left( \frac{V_B}{V_B + V_P} \phi_P + \frac{V_P}{V_B + V_P} \phi_B \right) \right\} \quad (4.23)$$

5 FEB 2003 / ME

पुरुषोत्तम क दीनाथ केवकर पुस्तकालय  
भा. भा. प्रौद्योगिकी संस्थान कानपुर

अवधि क्र० A 141972



A141972

In a fully implicit method the upwind parts of the above equations are implicit and they are incorporated in the coefficients of the unknown velocity during the pressure-velocity iterations. The CDS terms on the other hand are evaluated using the previous iteration values and used as a source term on the right side of the same equation. This is the so-called deferred correction approach of Khosla and Rubin (1974). Multiplication of the explicit part by a factor of  $\gamma$  ( $0 \leq \gamma \leq 1$ ) allows the introduction of numerical diffusion. For the first order upwind difference scheme,  $\gamma = 1$  and for the second order central difference,  $\gamma = 0$ . The deferred correction approach enhances the diagonal dominance of the coefficient matrix. However, the present solution scheme being explicit, the accuracy depends on the value of  $\gamma$ .

(c) **Diffusion Fluxes**

Peric(1985) calculated the expression for the diffusion fluxes in the finite volume approach. However, the exact expressions in three dimensions are not explicitly available in open literature. Eswaran and Prakash (1998) have evaluated the diffusion flux of a variable  $\phi$  through the cell faces in the following manner

$$\int_S \Gamma_\phi \nabla \phi \cdot dS \approx \sum_{j=e,w,n,s,t,b} (\Gamma_\phi \nabla \phi \cdot S)_j = \sum_j -F_j^d \quad (4.24)$$

For any face, Surface vector can be expressed as

$$S_j = \alpha_1 n^1 + \alpha_2 n^2 + \alpha_3 n^3 \quad (4.25)$$

Where  $n^1$ ,  $n^2$  and  $n^3$  are any three linearly independent (not necessarily orthogonal) unit vectors. Therefore

$$\nabla \phi \cdot S_j = \nabla \phi \cdot (\alpha_1 n^1 + \alpha_2 n^2 + \alpha_3 n^3) \quad (4.26)$$

$$= \alpha_1 \nabla \phi \cdot n^1 + \alpha_2 \nabla \phi \cdot n^2 + \alpha_3 \nabla \phi \cdot n^3$$

If  $\Delta\phi^1, \Delta\phi^2, \Delta\phi^3$  are the differences in  $\phi$  between the two ends of the line segments  $\Delta x^1, \Delta x^2, \Delta x^3$ , then

$$\Delta\phi^1 = \nabla\phi \cdot \Delta x^1, \quad \Delta\phi^2 = \nabla\phi \cdot \Delta x^2, \quad \Delta\phi^3 = \nabla\phi \cdot \Delta x^3 \quad (4.27)$$

If  $\Delta x^1, \Delta x^2, \Delta x^3$  are in the directions of  $n^1, n^2$  and  $n^3$  respectively, then it follows from equation (4.27) that

$$\frac{\Delta\phi^1}{\Delta x^1} = \nabla\phi \cdot n^1, \quad \frac{\Delta\phi^2}{\Delta x^2} = \nabla\phi \cdot n^2, \quad \frac{\Delta\phi^3}{\Delta x^3} = \nabla\phi \cdot n^3 \quad (4.28)$$

Where  $\Delta x^1, \Delta x^2$  and  $\Delta x^3$  are the magnitudes of  $\Delta x^1, \Delta x^2$  and  $\Delta x^3$ . Combining equations (4.26) and (4.28) we have

$$\nabla\phi \cdot S = \alpha_1 \frac{\Delta\phi^1}{\Delta x^1} + \alpha_2 \frac{\Delta\phi^2}{\Delta x^2} + \alpha_3 \frac{\Delta\phi^3}{\Delta x^3} \quad (4.29)$$

To obtain  $\alpha_1, \alpha_2$  and  $\alpha_3$ , we express

$$\begin{aligned} n^1 &= (n_{11} \ n_{12} \ n_{13}) \\ n^2 &= (n_{21} \ n_{22} \ n_{23}) \\ n^3 &= (n_{31} \ n_{32} \ n_{33}) \end{aligned} \quad (4.30)$$

Where  $n_{11}, n_{12}, n_{13}$  are the Cartesian components of  $n$  and which can be easily determined by  $\frac{\Delta x_1^1}{\Delta x^1}, \frac{\Delta x_2^1}{\Delta x^2}, \frac{\Delta x_3^1}{\Delta x^3}$ . The terms,  $\Delta x_1^1, \Delta x_2^1, \Delta x_3^1$  are the three components of vector  $\Delta x^1$ , etc. The other values  $n_{21} \dots n_{33}$  can be similarly obtained. Hence equation (4.29) can be written as

$$\begin{bmatrix} n_{11} & n_{12} & n_{13} \\ n_{21} & n_{22} & n_{23} \\ n_{31} & n_{32} & n_{33} \end{bmatrix}^T \begin{bmatrix} \alpha_1 \\ \alpha_2 \\ \alpha_3 \end{bmatrix} = \begin{bmatrix} S_{1j} \\ S_{2j} \\ S_{3j} \end{bmatrix}$$

Where  $S_{1j}$ ,  $S_{2j}$ ,  $S_{3j}$  are the Cartesian components of the surface vector  $S_j$ ,

Using Cramer's rule

$$\alpha_1 = \frac{D_1}{D}, \quad \alpha_2 = \frac{D_2}{D}, \quad \alpha_3 = \frac{D_3}{D} \quad (4.31)$$

Where  $D$  is the determinant of the coefficient matrix.  $D_1$  is obtained by replacing the first column of  $D$  by the column with the elements  $S_{1j}$ ,  $S_{2j}$ , and  $S_{3j}$ . Thus

$\alpha_1$ ,  $\alpha_2$ , and  $\alpha_3$  are determined.

The diffusion flux consists of two parts: normal derivative diffusion flux and cross derivative diffusion flux. The normal derivative flux of any dependent variable  $\phi$  through any cell face involves the values of  $\phi$  at cell centers whereas the cross-derivative diffusion flux involves the value of  $\phi$  at the edge center values. The normal derivative flux is treated implicitly and is coupled with the implicit part of the convective flux to calculate the main coefficients of the discretized equations while the cross-derivative diffusion flux is treated explicitly to avoid the possibility of producing negative coefficients in an implicit treatment. This term together with explicit part of convective flux is added to the source term. The example of the east face is taken to illustrate the diffusion model (Figure-4.3). Given the edge center values  $\phi_{te}$ ,  $\phi_{be}$ ,  $\phi_{se}$ ,  $\phi_{ne}$  we can get the

normal diffusion term  $\frac{\phi_E - \phi_P}{\Delta x^1}$ , and the cross diffusion term  $\frac{\phi_{te} - \phi_{be}}{\Delta x^2}$  and

$\frac{\phi_{se} - \phi_{ne}}{\Delta x^3}$ . Finally, the diffusion flux is computed by

$$F_j^d = -\Gamma_\phi \left( \alpha_1 \frac{\phi_E - \phi_P}{\Delta x^1} + \alpha_2 \frac{\phi_{te} - \phi_{be}}{\Delta x^2} + \alpha_3 \frac{\phi_{ne} - \phi_{se}}{\Delta x^3} \right) \quad (4.32)$$



For the evaluation of cross-derivative flux, the following interpolation scheme is used to obtain the edge center values

$$\phi_{te} = \frac{V_{TE}}{V_{tot}} \phi_P + \frac{V_P}{V_{tot}} \phi_{TE} + \frac{V_T}{V_{tot}} \phi_E + \frac{V_E}{V_{tot}} \phi_T \quad (4.33)$$

$$V_{tot} = V_{TE} + V_P + V_T + V_E$$

$$\phi_{be} = \frac{V_{BE}}{V_{tot}} \phi_P + \frac{V_P}{V_{tot}} \phi_{BE} + \frac{V_B}{V_{tot}} \phi_E + \frac{V_E}{V_{tot}} \phi_B \quad (4.34)$$

$$V_{tot} = V_{BE} + V_P + V_B + V_E$$

$$\phi_{ne} = \frac{V_{NE}}{V_{tot}} \phi_P + \frac{V_P}{V_{tot}} \phi_{NE} + \frac{V_N}{V_{tot}} \phi_E + \frac{V_E}{V_{tot}} \phi_N \quad (4.35)$$

$$V_{tot} = V_{NE} + V_P + V_N + V_E$$

$$\phi_{se} = \frac{V_{SE}}{V_{tot}} \phi_P + \frac{V_P}{V_{tot}} \phi_{SE} + \frac{V_S}{V_{tot}} \phi_E + \frac{V_E}{V_{tot}} \phi_S \quad (4.36)$$

$$V_{tot} = V_{SE} + V_P + V_S + V_E$$

Where,  $V_{TE}$  is the volume of the cell that is located at the top-east of the cell P. The other edge center values of the dependent variables can be interpolated in the similar way.

#### (d) Sources

The source term, which is integrated over the control volume, in the discretized equation can be considered as

$$\int_V S_\phi dV \approx (S_\phi)_P V \quad (4.37)$$

Apart from the real source  $S_\phi$ , explicitly treated parts of the convection and diffusion fluxes may be added to  $S_\phi$ . The pressure term in the momentum equations is also treated explicitly. Its discretization is analogous to that of the ordinary diffusion flux, i.e. for the  $i^{\text{th}}$  momentum equation the pressure term is

$$-\int_S p n_i S \approx \sum_j p_j S_{ij} \quad (4.38)$$

Where  $p_j$  is the pressure at the  $j^{\text{th}}$  face center and  $S_{ij}$  is the  $i^{\text{th}}$  component of the surface vector for space  $j$ .

#### 4.7 Pressure-Velocity Coupling

Simplified Marker and Cell (SMAC) method is used to obtain the velocity and pressure field that satisfies the mass and momentum equation. It is a semi-explicit method and it provides an efficient and easy way of pressure velocity coupling. The momentum equations are discretized in an explicit manner while the pressure gradient terms are treated implicitly, and the continuity equations are also enforced implicitly. Momentum and continuity equations can be expressed as

$$\rho V \frac{u_p^{n+1} - u_p^n}{\Delta t} + \sum_j (F^c + F^d)^n = - \sum_j p_j^{n+1} S_{ij} \quad (4.39)$$

and

$$\sum_j F_j^{n+1} = 0 \quad (4.40)$$

The momentum equations are solved using the guess values of velocity and pressure field. The provisional velocity components  $u_i^*$  are calculated from the following equation

$$u_p^* = u_p^o - \frac{\Delta t}{\rho V_p} (F_p^c + F_p^d) + \frac{\Delta t}{\rho V_p} S_{ii} \quad (4.41)$$

Where  $u_p^o$  is the value of velocity at earlier iteration and  $S_{ii}$  is the pressure term. This provisional velocity in general will not satisfy the continuity equation. The continuity equation (4.40) in another form reads as follows:

$$\begin{aligned} \sum_j (F_j^* + F_j') &= 0 \\ \sum_j F_j' &= - \sum_j F_j^* \end{aligned} \quad (4.42)$$

Where  $F_j^*$  is the uncorrected mass flux obtained from the provisional velocities and  $F_j'$  is the mass flux correction. To evaluate the terms on the right side of

equation (4.42), it is necessary that the variables (velocities and pressure) are to be known at the cell faces. Due to the non-staggered arrangement, if the variables at the cell faces are evaluated by linear interpolation between the adjacent cell center quantities then the pressure iteration does not converge. The solution leads to a Checker Board pressure field (i.e., spurious oscillation of pressure may occur), as shown by Rhie (1981). This problem can be circumvented by using the concept of Momentum Interpolation (Majumdar, 1988). The essence of the concept is that the velocities at the cell faces are computed by linear interpolation of the convective and diffusive terms but not the pressure term. Thus the method with the collocated variable arrangement relies indirectly on the staggering idea. Following this idea the interpolated velocity at the east face of the control volume given by is obtained in the following manner

$$u_e = \overline{(v_p, v_E)} - \frac{\Delta t}{\rho} \nabla p \quad (4.43)$$

Where

$$v_p = u_p^\circ - \frac{\Delta t}{\rho V_p} (F_p^c + F_p^d) \quad (4.44)$$

$$v_E = u_E^\circ - \frac{\Delta t}{\rho V_E} (F_E^c + F_E^d) \quad (4.45)$$

And the over bar indicates a linear interpolation using equation (4.16). So the uncorrected mass flux for the east face using equation (4.43) becomes

$$F_e^* = \rho u_e \cdot S_e = \rho \overline{(v_p, v_E)} \cdot S_e - \Delta t \nabla p \cdot S_e \quad (4.46)$$

Equation (4.46) in its generalized form for any cell face is in the form

$$F_j^* = \rho v_j \cdot S_j - \Delta t \nabla p_j \cdot S_j \quad (4.47)$$

To enforce mass conservation, the velocity and pressure corrections are introduced, linked by

$$u'_j = -\frac{\Delta t}{\rho} \nabla p'_j \quad (4.48)$$

This step simulates the effect of a staggered grid (face-center velocity and cell-center pressure) and reaps the benefits of faster convergence. From equation (4.48) we get the mass flux correction at the face j

$$F'_j = \rho u'_j \cdot S_j = -\Delta t \nabla p'_j \cdot S'_j \quad (4.49)$$

Since equation (4.49) is exactly of the same form as equation for diffusion flux equation (4.24), with only the variables interchanged, therefore the same method can be used for computing  $F'_j$

Combining equations (4.42), (4.47) and (4.49) yields

$$\begin{aligned} -\Delta t \nabla p'_j \cdot S_j &= \rho V_j \cdot S_j - \Delta t \nabla p_j \cdot S_j \\ \text{Or} \quad \Delta t \nabla p'_j \cdot S_j + S_m &= 0 \\ (S_m &= \rho V_j \cdot S_j - \Delta t \nabla p_j \cdot S_j) \end{aligned} \quad (4.50)$$

Which gives the *pressure* correction equation. After the solution of the pressure correction equation, the nodal velocity, mass fluxes and pressure are updated. The corrected pressure  $p^{n+1}$  is obtained by

$$p^{n+1} = p^n + p' \quad (4.51)$$

Instead of solving Equation (4.39) again with corrected pressure field, velocity correction can be calculated as follows

$$u'_p = -\frac{\Delta t}{\rho V_p} \sum_j p'_j S_{pj} \quad (4.52)$$

The corrected velocity field  $u_i^{n+1}$  is obtained by

$$u_i^{n+1} = u_i^* + u'_i \quad (4.53)$$

The energy equation is discretized and solved by using this new velocity distribution. On integrating the conservative form of the steady state energy equation over a control volume, neglecting the dissipative terms, as it is significant for high speed flows, the temperature equations becomes

$$\alpha \sum_j (\nabla T \cdot S)_j = \sum_j \rho u \cdot S_j T_j \quad (4.54)$$

which is solved by SOR method to get the temperature distribution at the current time step.

The first terms of equation (4.50) and equation (4.54) are expanded following the philosophy that was followed during the discretization of equation (4.24). Subsequent regrouping of the normal derivative terms yields the standard *Poisson Equation*. The Poisson equation can be solved by a multitude of methods. We have used the Gauss-Siedel iterative method, which is quite reliable and robust. The flow chart with the main steps of the algorithm is given in Figure 4.4.

#### 4.8 Solution Algorithm

The velocity pressure and temperature fields are calculated by the following the procedure of Eswaran and Prakash (1998). The procedure can be summarized in the following way:

1. Make initial guess of the pressure, velocity and temperature fields. Use equations (4.41) and (4.44) to calculate cell center  $\mathbf{u}_p$  and  $\mathbf{v}_p$ . Use linear interpolation equation (4.16) to obtain the face center quantities  $\mathbf{v}_j$ .
2. Compute the mass flux through cell face  $j$  using equation (4.47).
3. Use equation (4.48) to compute the flux correction at the cell face  $j$  using equation (4.49), which is computed using the formulation for diffusion fluxes [ Equations (4.24) to (4.36) ] For calculating by  $F_j'$ , the variable  $\phi$  is to be replaced by  $p'$ .
4. Compute the residue,  $\mathfrak{R}$  for each cell

$$\mathfrak{R} = - \sum_j F_j^* - \sum_j F_j'$$

- 5 Calculate the cell-center pressure correction (using Gauss-Siedel method) from the relation

$$p_p' = p_p' + \omega \frac{\mathfrak{R}}{a_p \Delta t}$$

where  $\omega$  is the relaxation factor and  $a_p$  stands for the diagonal coefficients of equation (4.50), which is calculated from

$$a_p = - \left[ \frac{\alpha_1}{\Delta x^1} \Big|_w - \frac{\alpha_1}{\Delta x^1} \Big|_e + \frac{\alpha_2}{\Delta x^2} \Big|_n - \frac{\alpha_2}{\Delta x^2} \Big|_s + \frac{\alpha_3}{\Delta x^3} \Big|_s - \frac{\alpha_3}{\Delta x^3} \Big|_t \right]$$

where  $\alpha_1, \alpha_2$  etc are the same as that are used in equation (4.24) to (4.36).

6 If  $\mathfrak{R}_{ms} > \varepsilon$  go to step 3.

7 Store the updated mass flux through cell faces using equation (4.47).

8 Store the updated pressure at the center of the cells

$$p_p = p_p + p'_p$$

9 Store the cell-center corrected velocity

$$u'_p = -\frac{\Delta t}{\rho V_p} \sum_j p'_j S_{ij}$$

$$u_i^{n+1} = u_i^* + u'_i$$

10 Calculate the residual for each cell

$$\tilde{\mathfrak{R}} = \alpha \sum_j (\nabla T \cdot S)_j = \sum_j \rho u \cdot S_j T_j$$

11 Calculate the cell-center temperature using Gauss-Seidel method to obtain

$$T_p = T_p + \Omega \frac{\tilde{\mathfrak{R}}}{b_p \alpha}$$

Where  $\Omega$  is the relaxation factor and  $b_p$  stand for the diagonal coefficients of equation (4.54) i.e., calculated from the relation

$$b_p = -a_p$$

12 If  $\tilde{\mathfrak{R}}_{ms} > \varepsilon$  go to step 10.

13 Go to step 1 and repeat the process until the steady state is reached. It can be shown that solving equation (4.42) is same as solving

$$\nabla^2 p' = -\rho \frac{\nabla \cdot u_j^*}{\Delta t}$$

and finding the corrections

$$u'_j = -\frac{\nabla t}{\rho} \nabla p'$$

such that

$$u_i^{n+1} = u_i^* + u'_i$$

$$p^{n+1} = p^n + p'$$

Thus the procedure above can be called solution of *Pressure Correction Linked Equations*.

#### 4.9 Numerical Stability Considerations

Semi-Explicit method used for present computations relies on explicit differences and impose certain restrictions on time step. For a given mesh the choice of time step is determined through stability analysis, which has to take care of two conditions. First, fluid should not be allowed to cross more than one cell in any one-time step. This restrictions is derived from the Courant-Friedrichs-Lewy (CFL) conditions given by

$$\delta t_1 < \min \left\{ \frac{\delta x}{|u|}, \frac{\delta y}{|v|}, \frac{\delta z}{|w|} \right\} \quad (4.55)$$

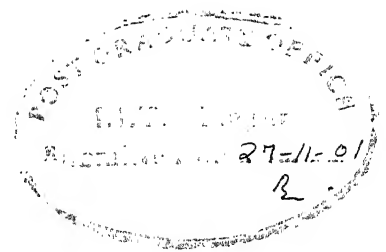
Where the minimum is with respect to every cell in the domain. Typically  $\delta t_1$  is chosen equal to one-third to two-third of the minimum cell transient time.

Secondly, when a non-zero value of kinematic viscosity is used momentum must not diffuse more than approximately one cell in one time step. A linear stability analysis shows that the restrictions on grid Fourier number will yield

$$\delta t_2 < \frac{1}{2} \frac{(\delta x)^2 (\delta y)^2 (\delta z)^2}{(\delta x)^2 + (\delta y)^2 + (\delta z)^2} \text{Re} \quad (4.56)$$

Finally, the minimum of the two above time increments is chosen for computation.

# Certificate



This is to certify that the thesis entitled **“Winglet-type vortex generators with common-flow-up configuration for fin-tube heat exchangers”** by Mr. Aseem Jain has been carried out under my supervision. The contents of this thesis have not been submitted to any other institute or university for the award of any degree or diploma.

*Gautam Biswas*

Dr. Gautam Biswas

Professor

Department of Mechanical Engineering

Indian Institute of Technology

Kanpur-208016

November 27, 2001



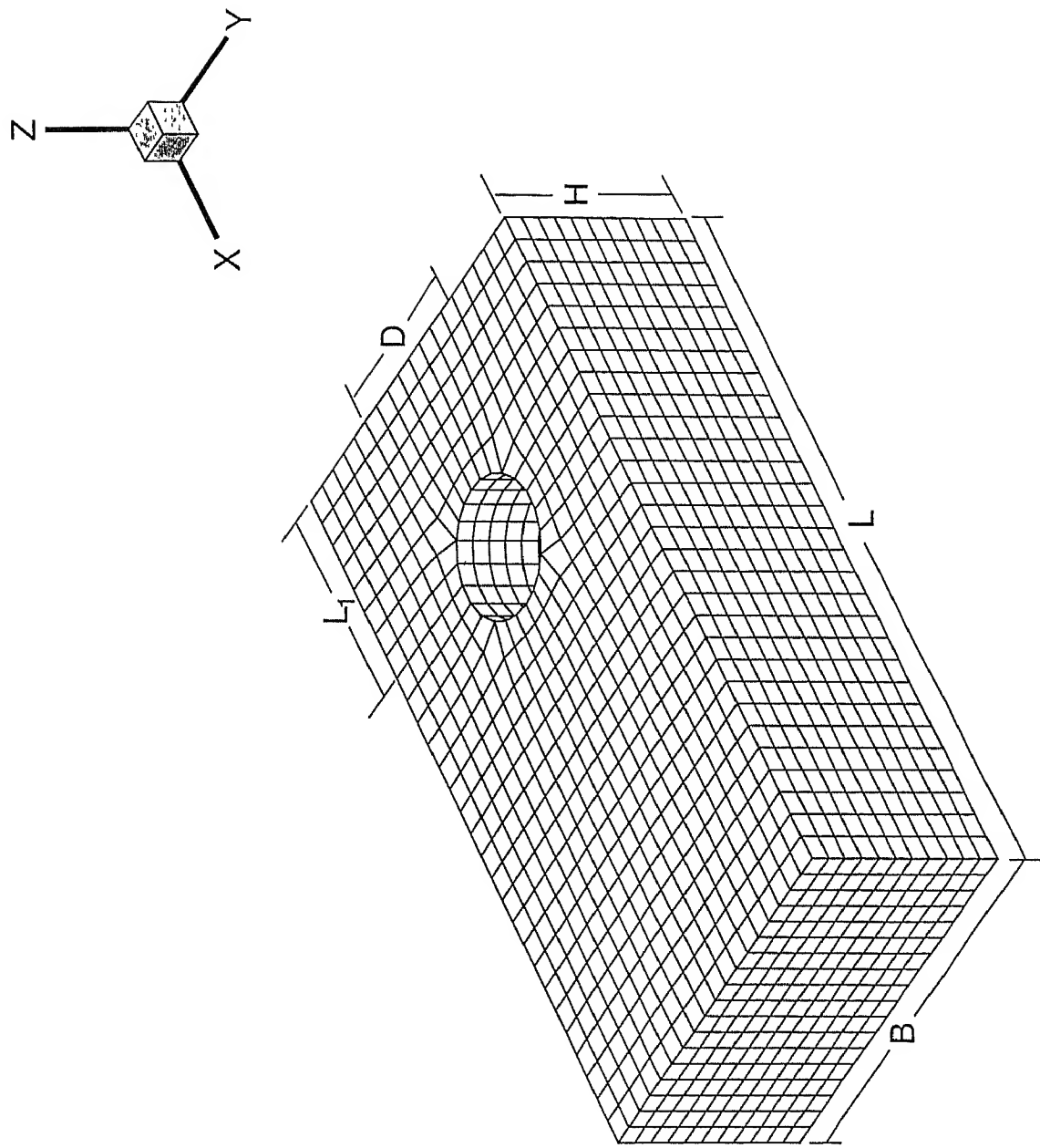


Figure 4.1 Schematic of grid mesh and computational domain

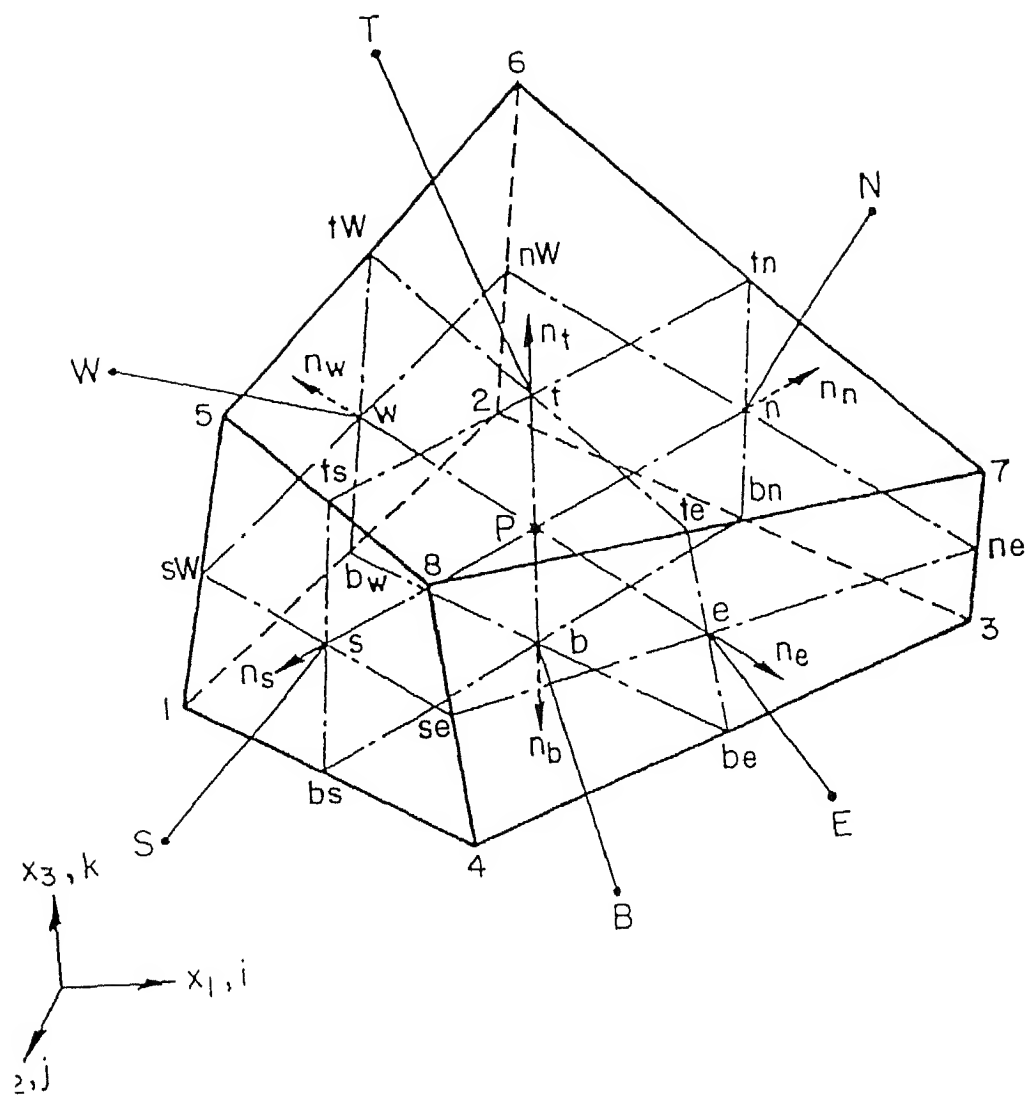


Figure 4.2 Three-dimensional finite volume cell

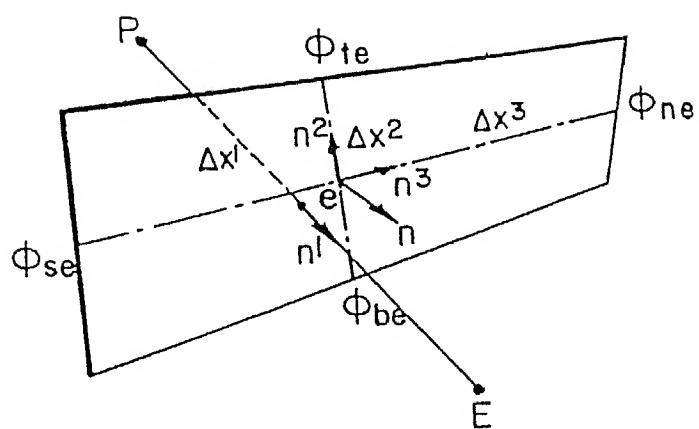


Figure 4.3 Face representation to illustrate the diffusion model

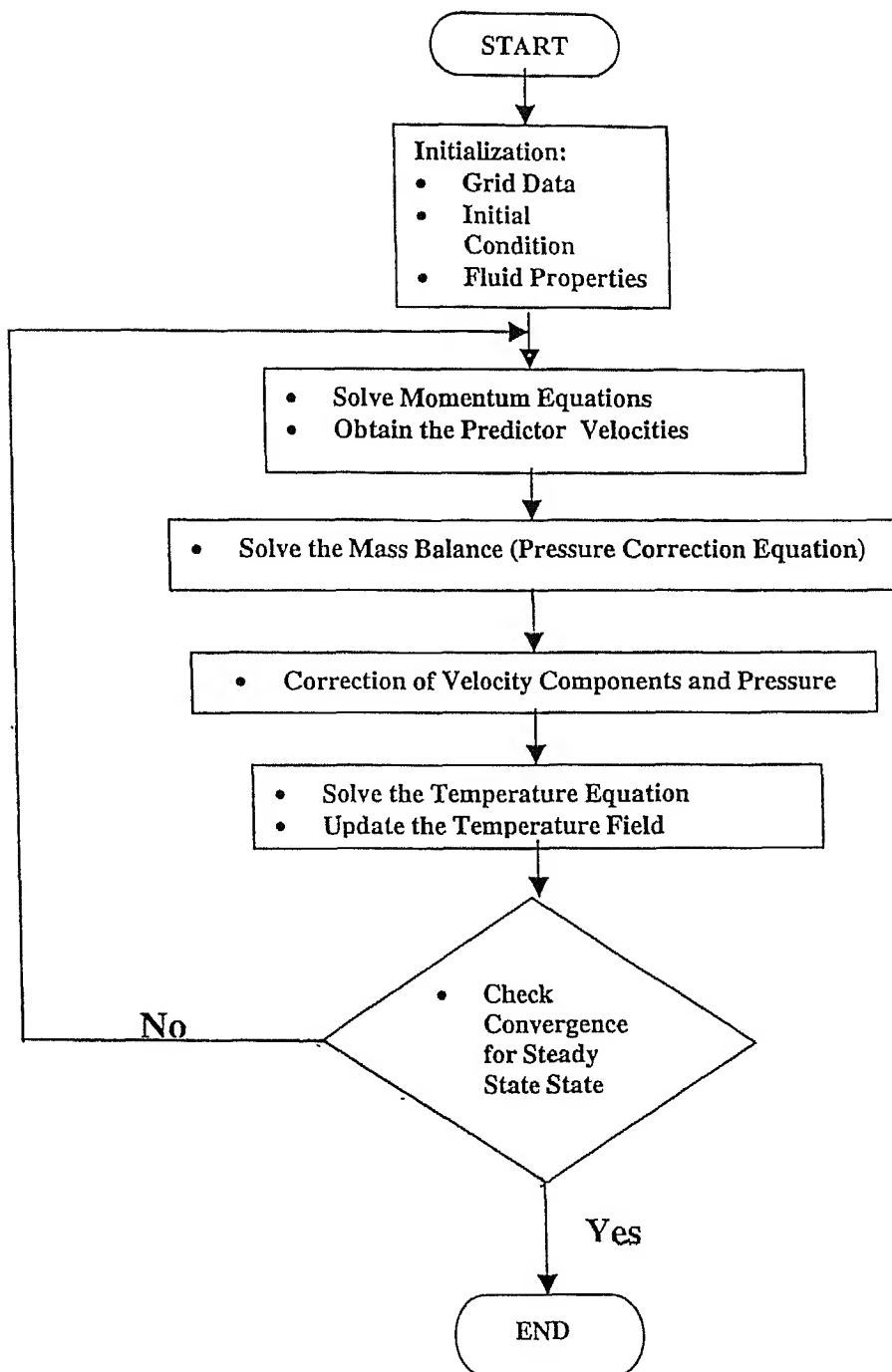


Figure 4.4 Flowchart of iterative solution scheme

## Chapter 5

### Results and Discussion

#### 5.1 Introduction

A three dimensional numerical solution of flow and heat transfer for a plane channel with built in circular tube and delta winglet pair in common-flow-up configuration is presented in this section. A  $74 \times 48 \times 23$  grid-mesh is used in the present computation. The divergence-free criterion is satisfied using an upper bound of  $10^{-4}$ . Computations have been carried out for moderately high Reynolds numbers in the range of 1000 and 1350. Air has been taken as the working fluid; hence the Prandtl number of the present study is 0.7. The Nusselt number is calculated on the basis of bulk mean temperature. D/B has been kept constant equal to 0.36 for all computations.

#### 5.2 Flow and Heat Transfer Characteristics in a Rectangular Channel with a built-in Circular Tube

A detailed analysis of flow and heat transfer characteristics in a rectangular channel with a built-in circular tube is presented herein. The results presented here are for a Reynolds number of 1000.

##### 5.2.1 Flow Characteristics

Figure 5.1 (a) shows limiting streamlines near the bottom wall for the instantaneous flow field in a channel with a built-in circular tube. A saddle point of separation and a horseshoe vortex system is observed in the figure. The incoming flow reaches a stagnation or saddle point of separation (marked by A) and goes around the body. The nodal point of attachment (marked as C) and the separation lines are also visible. On each side of the tube, one finds a region of

converging streamlines (marked as G). These are the traces of horseshoe vortices. The symbol E marks the footprints of shed vortices. Figure 5.1 (b) shows the limiting streamlines close to the bottom for the time-averaged flow field. The traces of symmetric vortices are seen in the figure.

Figures 5.2 (a) through 5.2-(f) show vortex shedding past the tube at the horizontal midplane of the channel. The sequence of events in the figure reveals that the vortex from the bottom side of the tube is shed into the stream while another vortex grows at that same location to the limit of onset of shedding. Likewise, Figures 5.3 (a) through 5.3-(f) show the shedding of the vortex from the topside of the tube. Figure 5.4 shows the streamlines for the time-averaged flow on the horizontal midplane.

### 5.2.2 Heat Transfer Characteristics

Figure 5.5 represents the Nusselt number distribution on the bottom plate of the channel with a built-in circular tube for the Reynolds number of 1000. The following regimes may be distinguished. At the leading edge of the bottom plane, Nusselt number starts with a high value and decreases gradually. At the leading edge of the plate, the cooler fluid comes in contact with the hot fin for the first time hence the heat transfer is very high. The gradual decrease in the Nusselt number is attributed due to the development of thermal boundary layer on the channel walls. In front of the tube, a zone of high Nusselt Number is observed. This increase in Nusselt number results from the formation of the horseshoe vortex system that consists of two counter-rotating longitudinal vortices. As the fluid approaches the stagnation line of the circular tube, it slows down and its pressure increases. The smaller velocity within the boundary layer in the vicinity of the bottom plate, which supports the circular tube, leads to a smaller pressure increase. Thus, the induced pressure gradient on the stagnation line causes the flow towards the bottom wall that interacts with the main stream. The fluid rolls up forming vortices, which finally wraps around the front half of the tube and

extends to the rear of the tube (Goldstein and Karni (1984)). The horseshoe vortices generated in front of the tube bring about better mixing and the heat transfer in this region is enhanced significantly. The Nusselt number is low in the wake region. The poor heat transfer in this region is attributed to the separated dead water zone with fluid recirculating at a low velocity.

### **5.3 Effect of Winglet-Pair on Flow and Heat Transfer**

Detailed analysis of flow structure and heat transfer characteristics in a channel with a built-in tube along with winglet pair placed in common-flow-up configuration is presented herein. The results presented correspond to a Reynolds number of 1000. Different values of transverse distance between the trailing edges of the winglets have been considered. However, generally  $b/D = 1.08$  for delta winglet and  $b/D = 1.67$  for rectangular winglet, if it is not mentioned otherwise in the text.

#### **5.3.1 Flow Characteristics**

Figure 5.6 shows the limiting streamlines for the velocity field on a horizontal plane close to the bottom wall with winglets placed in common-flow-up configuration behind the tube. If one considers the flow passage between one of the winglets and the curved surface of the tube, the geometrical shape resembles a nozzle like configuration. The fluid layers do not face adverse pressure gradient in the aft of the circular tube. Instead, the fluid accelerates in the constricted passage and the wake region becomes quite narrow. The winglet pair causes transverse motion, which in turn delays the separation. Separation is not observed till a separation angle of  $170^\circ$ . A very narrow wake is formed indicating F as the wake stagnation point.

Figure 5.7 shows streamline plot on the horizontal mid-plane with winglets in common-flow-up configuration. Symmetry can be clearly observed even in an instantaneous flow field in this case as vortex shedding is suppressed.

Figure 5.8 shows streamlines on the vertical mid-plane with winglets placed behind tube in common-flow-up configuration. The formation of horseshoe vortices in front of the tube is evident from this figure. Placing of winglets stops the vortex shedding and creates a strong swirling motion behind the tube. The swirl is primarily characterized by a longitudinal vortex system. The projection of this complex structure is observed on the vertical plane behind the tube.

Figures 5.9 (a), (b) and (c) show cross-stream velocity vectors at various axial locations in the channel with the circular tube and the winglet pair as the built-in obstacles. Schematic location of the winglet pair has already been shown in Figure 1.2. The axial location of Fig. 5.9(a) is near the trailing edge of the winglet pair. The velocity vectors depict the secondary flow pattern on various cross-stream planes in the channel. The results correspond to a Reynolds number of 1000 and an angle of attack of  $138.61^\circ$ . The pressure difference between the front surface, facing the flow and the suction surface of the winglet generates swirling motion. The swirling motion is described by the longitudinal vortices. The figure clearly reveals that the crossflow pattern depicts a common-flow-up situation. Mendez et al. (1998) have explained the kinematics of flow and the mechanism of transport enhancement due to longitudinal vortices. The strength of the vortex motion decreases with the downstream distance from the winglet. The decrease in vortex strength can be attributed to viscous diffusion.

Figures 5.10 (a), (b) and (c) show cross-stream velocity vectors at same axial locations in the channel but with rectangular winglet of same aspect ratio (double the area of the delta winglet), instead. At the same axial location, the vortex strength described by the rectangular winglet is higher as compared to the delta winglet. The surface area of the rectangular winglet is more than that of the delta winglet.

Figures 5.11(a), (b), (c) and Figures 5.12(a), (b), (c) represent the streamlines on the cross-stream plane at the non-dimensional axial locations of 10.17, 13.75 and 17.32 from the leading edge of the channel for the delta and rectangular winglets respectively. The streamlines confirm existence of a strong vortical motion that



was explained through Figures 5.9 and 5.10. The centers of the main vortices of the longitudinal vortex system are located at distance of  $\pm 0.3B$  from the vertical midplane. Induced vortices become prominent as the pair of longitudinal vortices travel in the downstream.

The lateral distance between the winglet pair has been varied to observed its effect on the vortical motion. The lateral distance between the trailing edges is given by  $b$ . For the cases, described in Figures 5.9 and 5.10, the parameter  $b/D$  is taken as 1.67. For the delta winglet pairs and  $b/D$  of 1.08, Figs 5.13 (a), (b) and (c) have described the vortical motion at three different cross-stream planes. One can see that the main vortices of the longitudinal vortex system have come closer to each other due to reduced  $b/D$ .

Figures 5.14, 5.15 and 5.16 show three-dimensional particle paths for the delta and rectangular winglets placed in common-flow-up configuration. Complex vortex structures generated due to the configurations of interest are clearly visible in these figures. All the figures show generation of horseshoe vortices in front of the tube. The generation longitudinal vortices due to the delta winglet pair with  $b/D = 1.67$  has been shown in Figure 5.14. Likewise, Fig. 5.15 shows the generation of longitudinal vortices due to the rectangular winglet pair. Figure 5.16 displays the vortical structure due to delta winglet pair with  $b/D = 1.08$ .

### 5.3.2 Heat Transfer Characteristics

Nusselt number distribution at bottom plate of channel with winglets placed in common-flow-up configuration is shown in Figure 5.17. From entrance of the channel, till the axial location of the leading edge of winglet pair, the variation of  $Nu$  is same as Figure 5.5. Beyond this location, the Nusselt number starts increasing. A sharp rise in Nusselt number is observed near the location of the trailing edge of the winglet. This enhancement is attributed to the formation of a complex vortex system that consists of two counter-rotating longitudinal vortices.

The formation of longitudinal vortices brings about a better mixing and the Nusselt number becomes high in the zone influenced by the swirl.

Figure 5.18 compares the span-averaged Nusselt number distribution on the bottom wall in a channel for the cases of built-in circular tube, without and with winglet pair. The Reynolds number of interest is 1000. The span-averaged Nusselt number reaches the maximum value near the axial location of the leading edge of the circular tube. This is primarily governed by the formation of horseshoe vortices at the tube and bottom wall junction as explained earlier. The peak value of the span-averaged Nusselt number is about 11.2. Up to the location of the leading edge of the winglets, the distribution of span-averaged Nusselt number is almost same for the cases with and without winglets. However, beyond that location, Nusselt number starts increasing for the case of built-in winglet pair. The maximum enhancement in heat transfer (95 percent) takes place at the immediate upstream of the trailing edge of the winglet pair ( $X = 9.8$ ). At the exit of the channel, the span-averaged value of Nusselt number is 5.8. The span-averaged Nusselt number value at the exit ( $X = 20$ ) of a plane channel is 4.0 while for the case of a channel with a built-in circular tube, it is 3.7.

Figure 5.19 compares the distribution of span-averaged Nusselt number on the bottom wall of channel for two Reynolds numbers, namely  $Re = 1000$  and  $Re = 1350$ . As expected, the Nusselt number distribution is higher for the higher Reynolds number.

Figure 5.20 compares the distribution of span-averaged Nusselt number on the bottom wall of the channel with a built-in circular tube for cases of delta and the rectangular winglet pair as the second obstacle. The Nusselt number distribution is higher for the rectangular winglet pair as compared to the delta winglet pair. The surface area of the rectangular winglet pair being more (due to same aspect ratio of two different types of winglets), the strength of the vortical motion in the case of rectangular winglet pair is high.

Figure 5.21 shows the distribution of span-averaged Nusselt number on the bottom wall of the channel with built-in circular tube for the cases of delta

## **Abstract**

Numerical investigation of flow and heat transfer in a rectangular channel with built-in circular tube and different types of winglets placed in common-flow-up configuration has been carried out. The Reynolds numbers are moderately high, in the range of 1000. Existing air-cooled condensers in geothermal power plants use fin-tube heat exchangers with circular tubes. The size of the heat exchangers is huge and often the cost of the condensers is more than one-third of the plant cost. The size of the condensers can be reduced through enhancement of heat transfer from fin surfaces. The enhancement strategy involves introduction of strong swirling motion in the flow field. The swirl can be generated by the longitudinal vortices. In this study, the longitudinal vortices are created by the winglet type vortex generators, which are mounted behind the tubes. An element of a heat exchanger has been considered for detailed study of the flow structure and heat transfer analysis.

In the present study, a novel technique (Torii et. al., 2000) has been utilized for the enhancement of transport coefficients. The winglets are placed with a heretofore-unused orientation for the purpose of augmentation of heat transfer. This orientation is called as common-flow-up configuration. The proposed configuration causes significant separation delay, reduces form drag, and removes the zone of poor heat transfer from the near-wake of the tubes. The analyses of flow and heat transfer in the proposed configuration have been accomplished through a numerical solution of complete Navier-Stokes and energy equations.

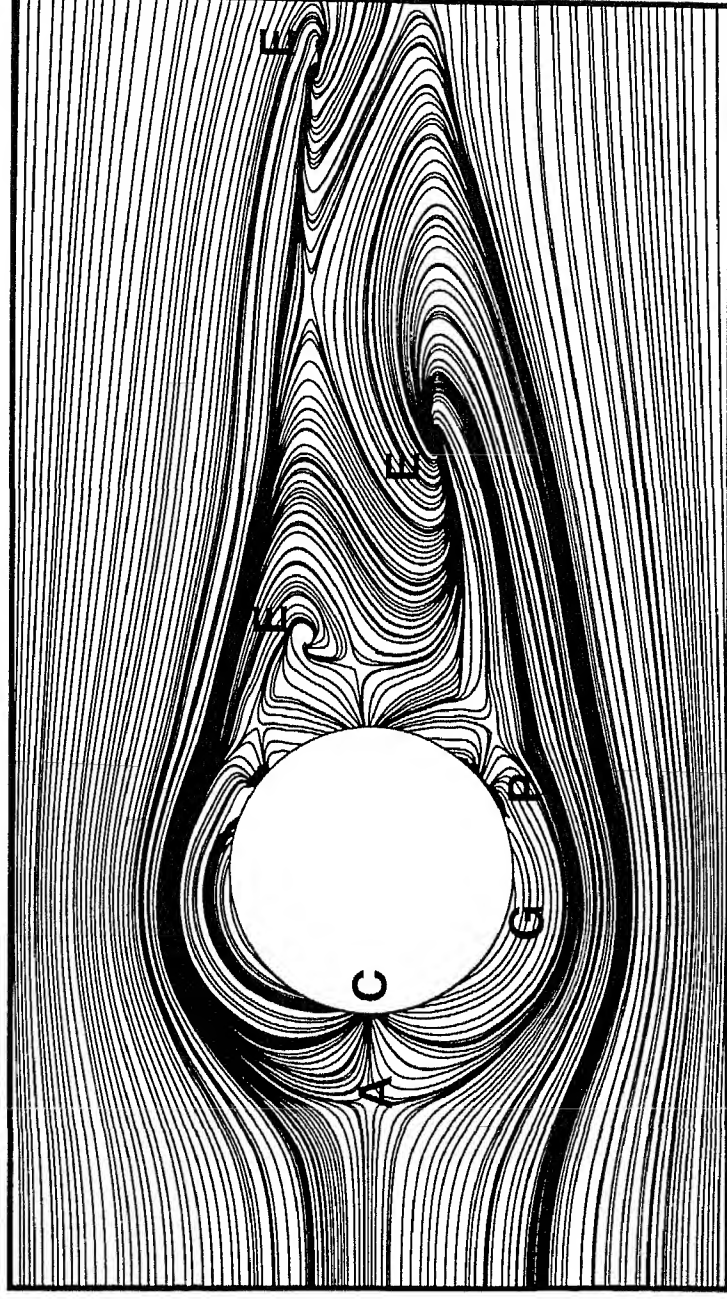
winglets with different transverse distances between their trailing edges. The span-averaged Nusselt number distribution is almost same for the two situations, mentioned above. For the case of lateral distance  $b=1.08D$ , the span-averaged Nusselt number increases in the wake region of the winglets, whereas the span-averaged Nusselt number is slightly less near the leading edge as compared to the case of  $b=1.67D$ .

#### 5.4 Spatial Grid Independence Model Validation

Spatial Grid independence test has been carried out using two grid-meshes of sizes  $74 \times 48 \times 23$  and  $60 \times 48 \times 20$ . Figure 5.22 shows span-wise average Nusselt number distribution for two grid-meshes. They compare favorably indicating the grid-independent situation for the grid size of  $74 \times 48 \times 23$ .

The code validation was accomplished through comparison with the experimental results of Torii (2001). Figure 5.23 compares the present computation with the experimental results of Torii (2001). The enhancement is expressed in terms of the ratio of the ratio of  $\overline{Nu}_s$  and  $\overline{Nu}_{so}$ . Here  $\overline{Nu}_s$  is the span-averaged Nusselt number at any axial location for the case of a channel with built-in circular tube and winglet pair and  $\overline{Nu}_{so}$  is the span-averaged Nusselt number at any axial location for the case of a channel with a built-in circular tube. The axial location of the center of the tube has been taken as the reference coordinate point in the figure. The Reynolds number of interest is 1320 and the experimental technique of heat transfer measurement is based upon the experimental study of Mochizuki et al (1988). The computation and experimental results compare well in general, and in the downstream of the trailing edge in particular.

$Re = 1000$        $Pr = 0.7$



L

Figure 5.1(a) Limiting streamlines based upon instantaneous flow on a plane close to the bottom plate for a channel with built-in circular tube

$Re = 1000$        $Pr = 0.7$

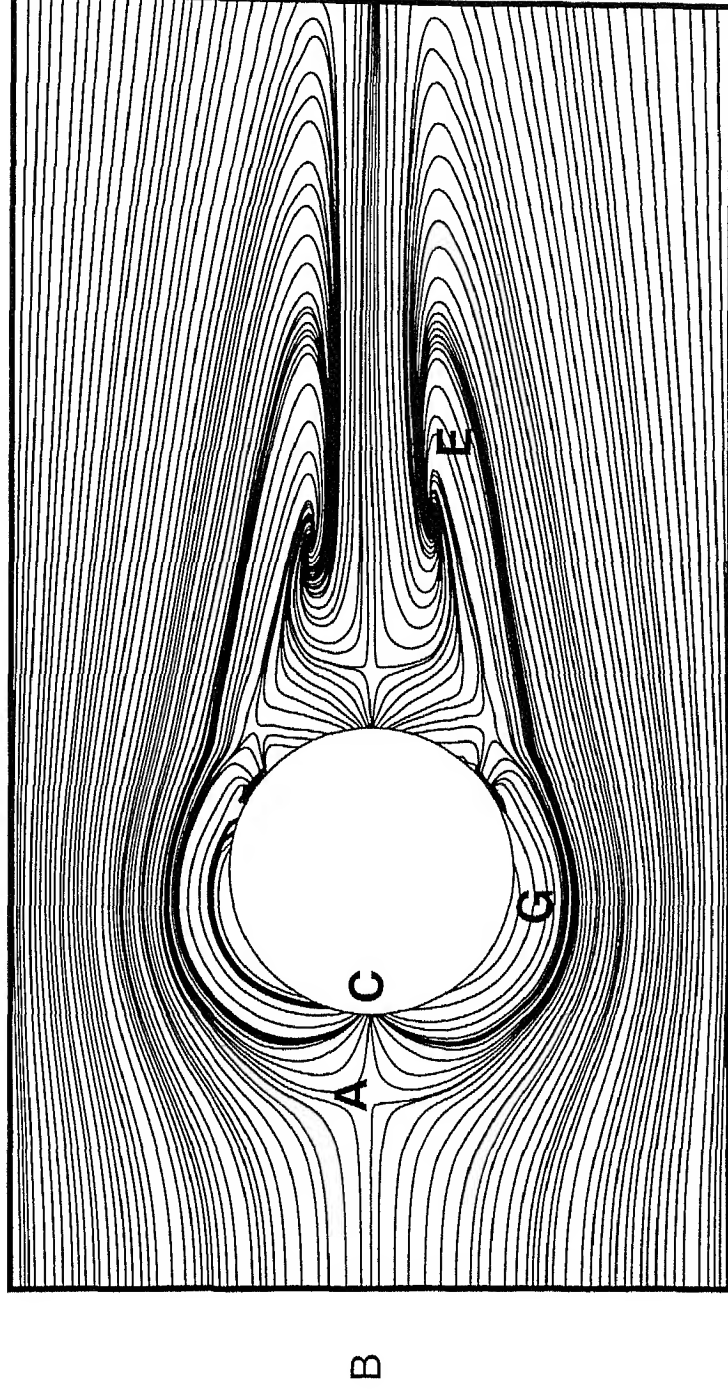


Figure 5.1(b) Limiting streamlines based upon time averaged flow on a plane close to the bottom plate for a channel with built-in circular tube

$Re = 1000$

$Pr = 0.7$

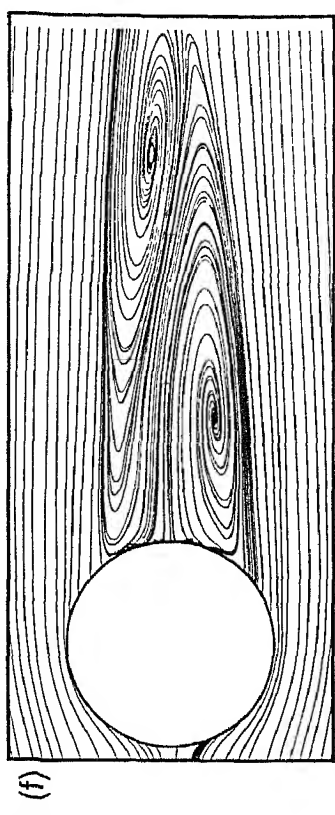
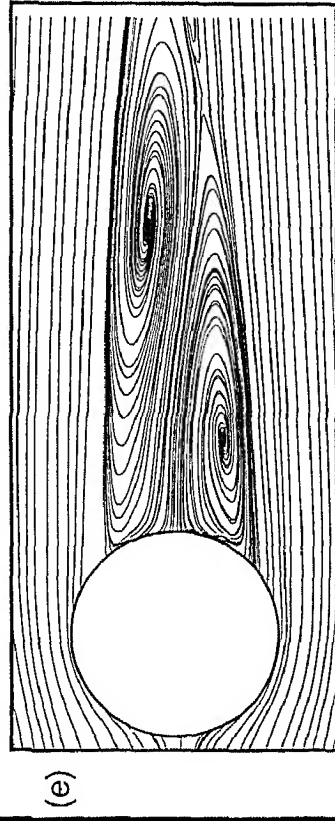
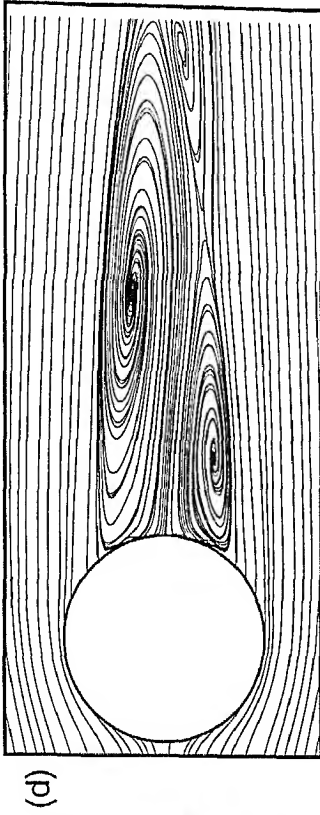
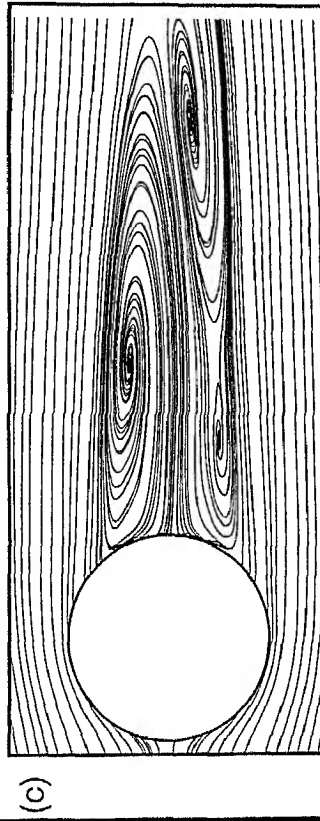
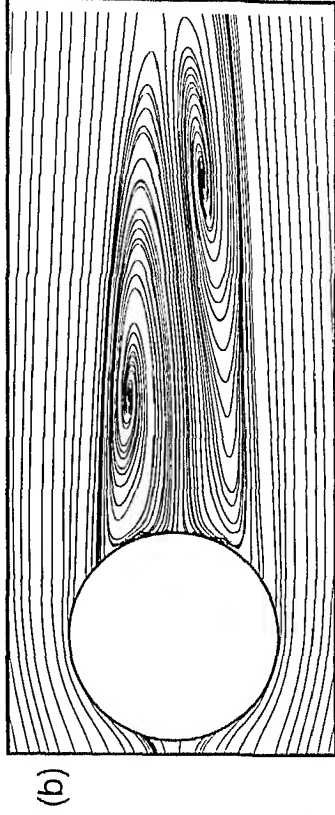
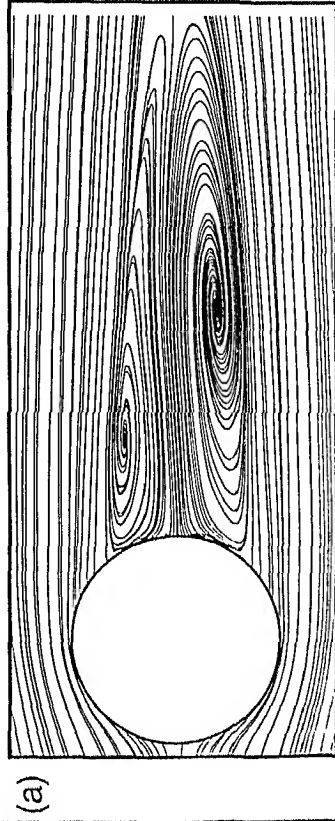


Figure 5.2 Vortex shedding at mid-plane in the wake of circular tube

$Pr = 0.7$

$Re = 1000$

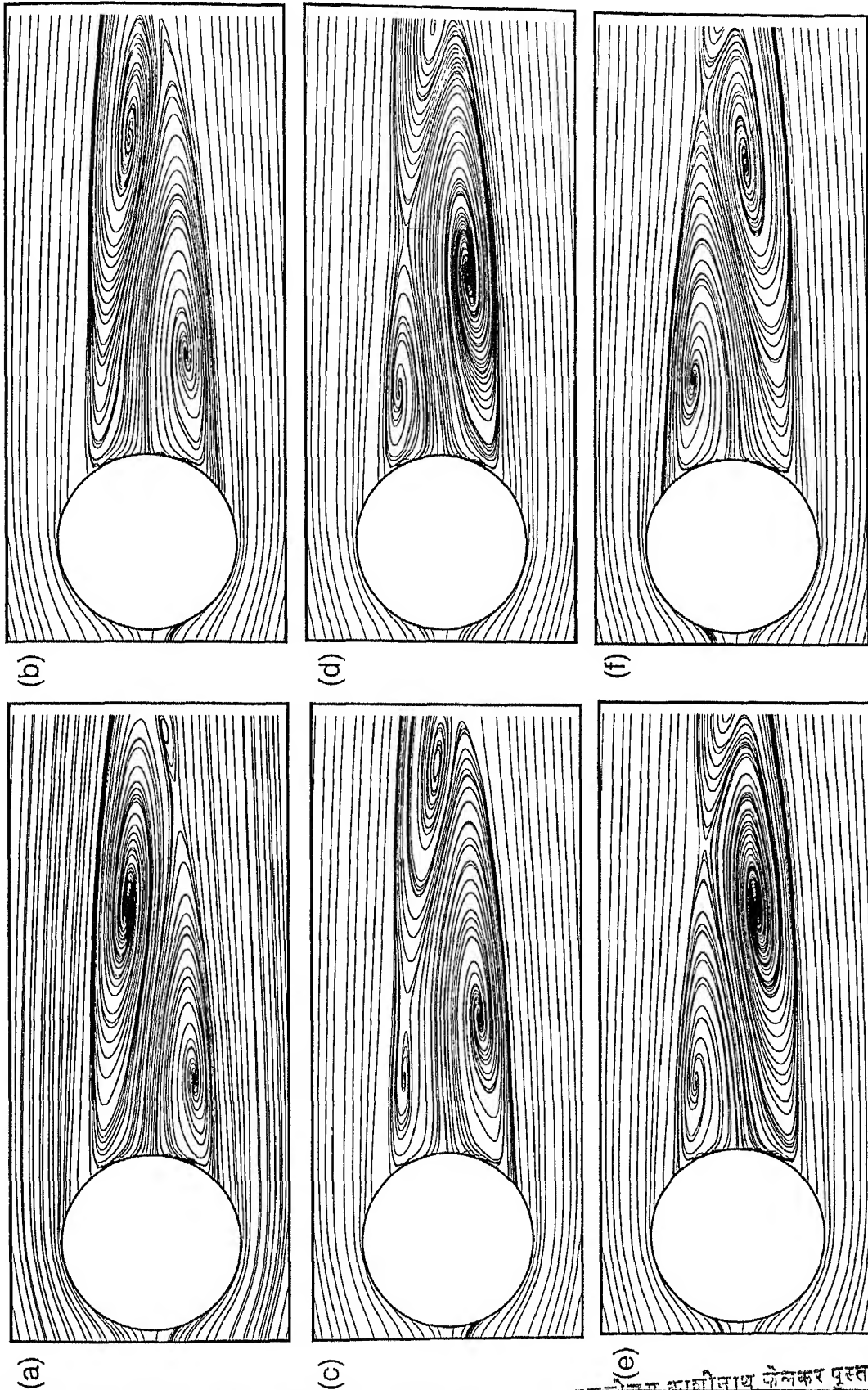
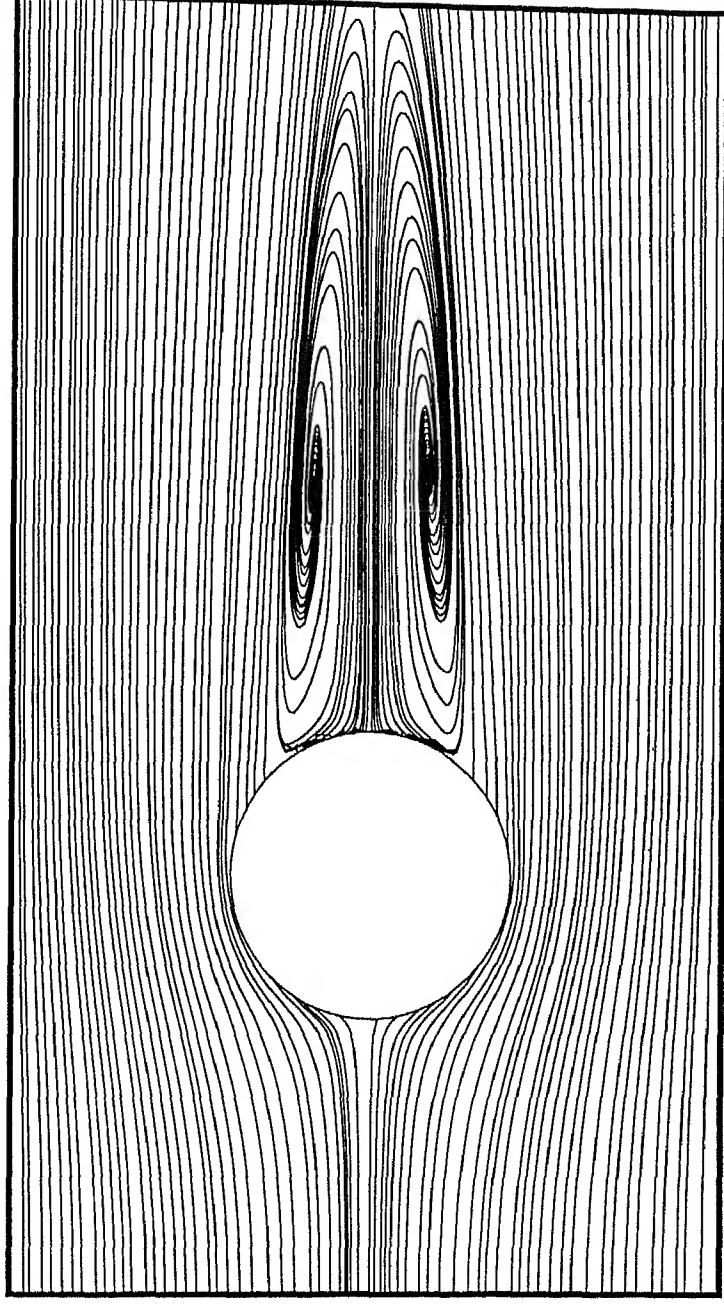


Figure 5.3 Vortex shedding at mid-plane in the wake of circular tube



$Re = 1000$        $Pr = 0.7$

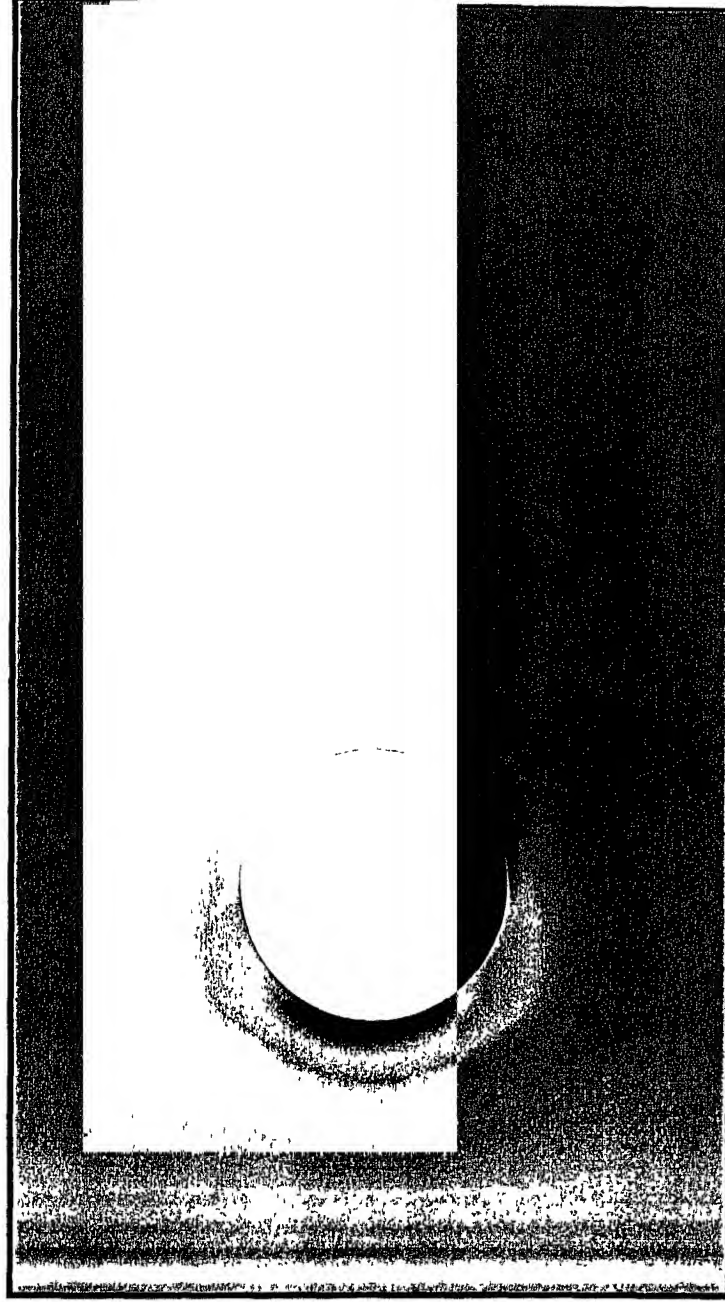


L

Figure5.4 Streamline plot for time averaged flow on a horizontal mid-plane  
Of a channel with built-in circular tube

$Re = 1000$

$Pr = 0.7$



B

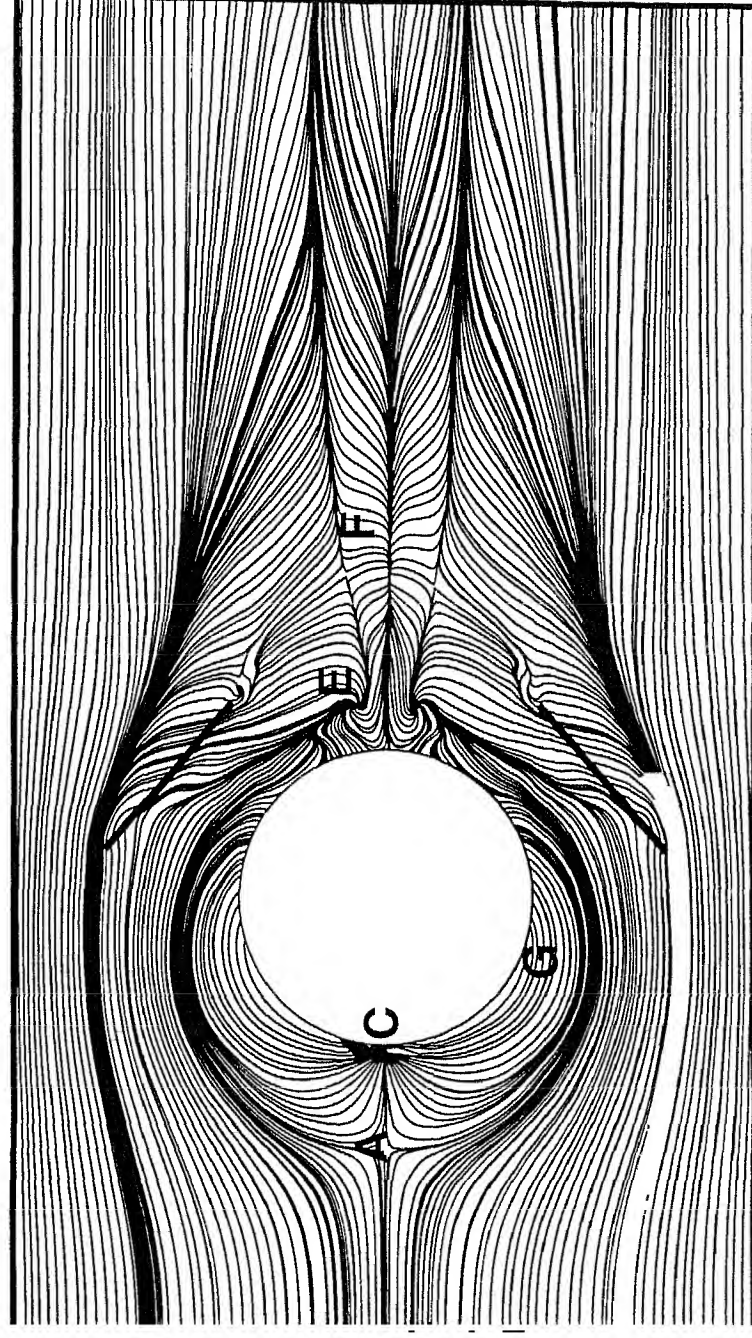
L

Nu

	0	4.51128	9.02256	13.5338	18.0451	22.5564	27.0677	31.5789

Figure 5.5 Nusselt number distribution on the bottom plate of a channel with built-in circular tube

$Re = 1000$        $Pr = 0.7$        $\beta = 138.61^\circ$



L

Figure 5.6 Limiting streamlines on a plane close to the bottom plate for a channel with built-in circular tube and a pair of delta winglets in common-flow-up configuration

$Re = 1000$        $Pr = 0.7$        $\beta = 138.61^\circ$

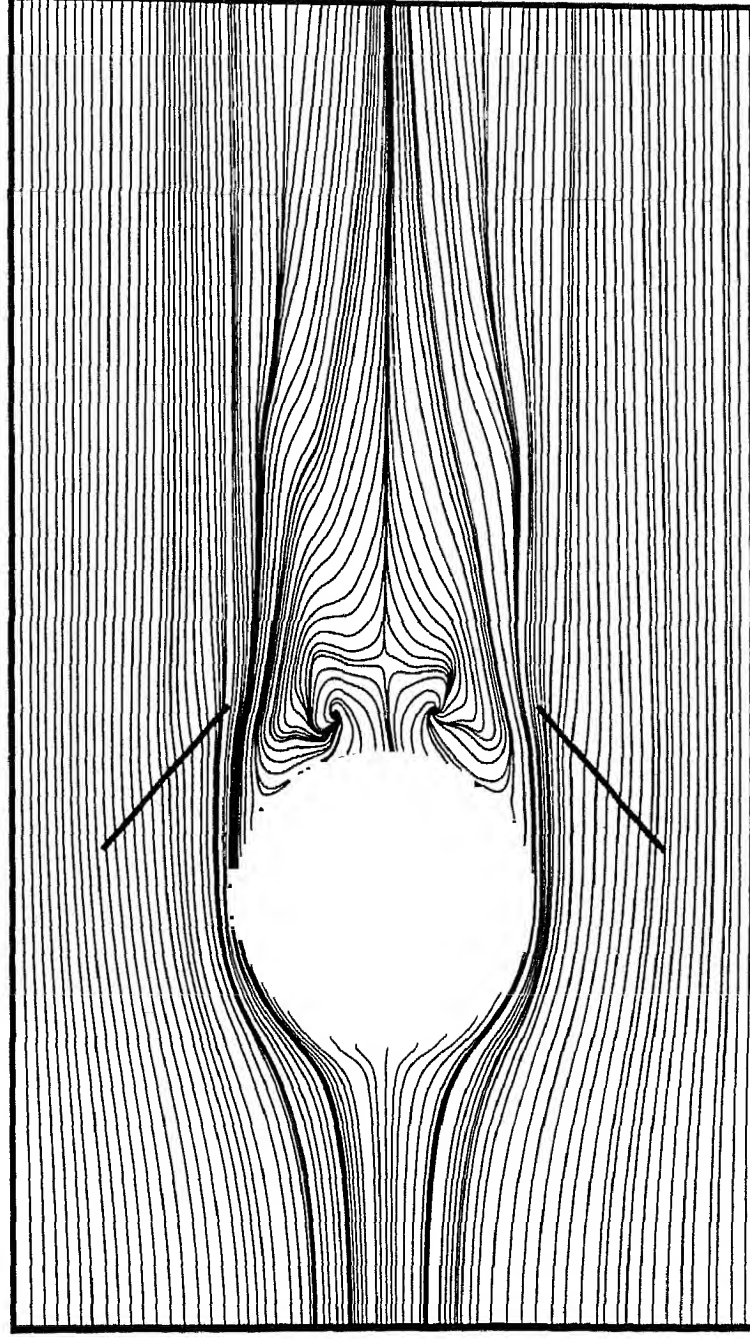


Figure 5.7 Streamline-plot on the horizontal midplane of a channel with built-in circular tube and delta winglet-pair in common-flow-up configuration

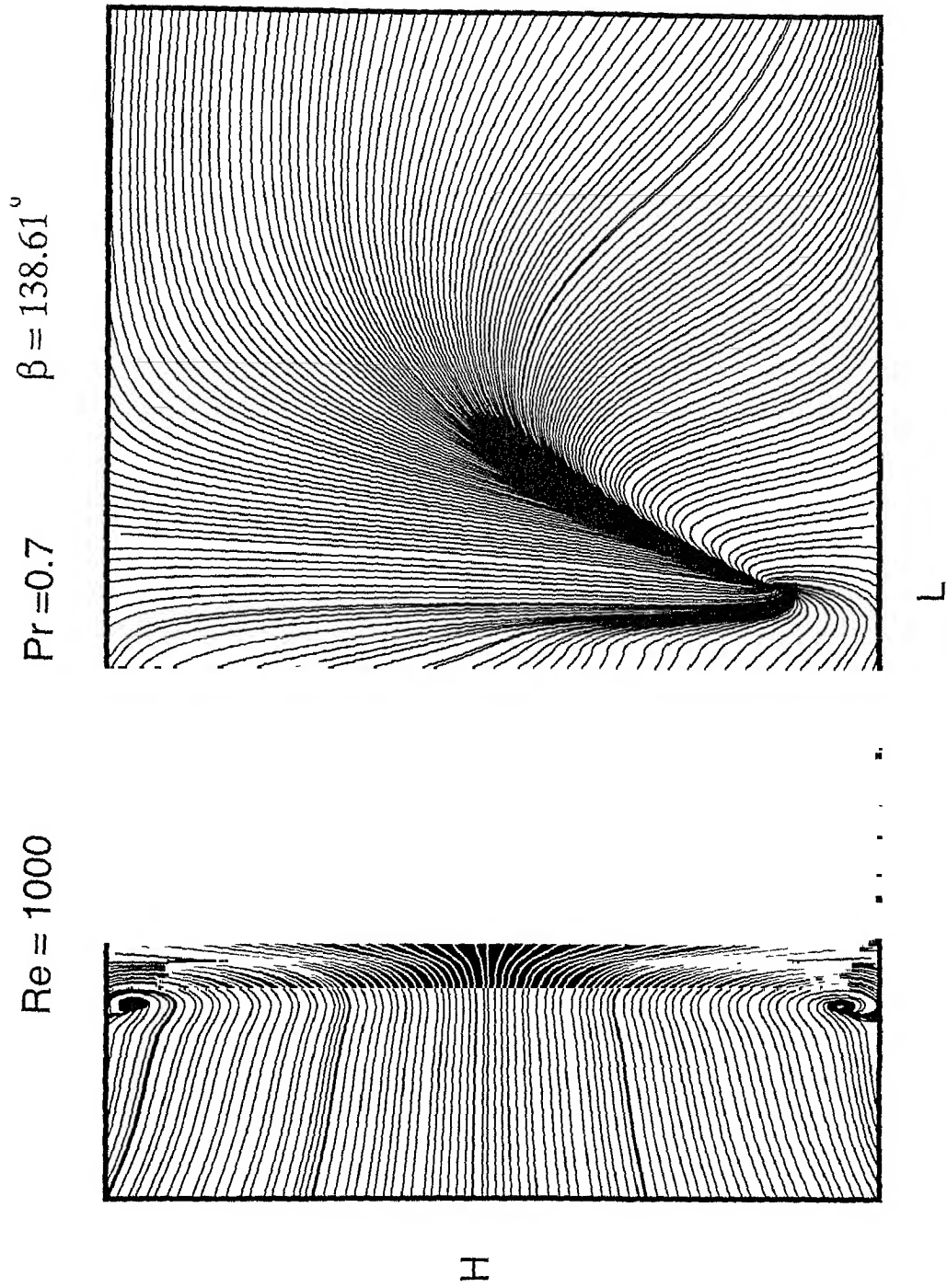


Figure 5.8 Streamline-plot on the vertical midplane of a channel with built-in circular tube and delta winglet-pair in common-flow-up configuration

## ACKNOWLEDGEMENTS

During the journey towards completion of this work, many people have contributed directly or indirectly. I take this opportunity to thank all of them.

I feel very fortunate to have Dr. Gautam Biswas as my thesis supervisor. Without his invaluable suggestions my thesis could have not come to this stage. His amicable personality always gave me pleasure to have discussions with him regarding thesis or any personal matter. I cherish each and every moment I spent with him.

I would like to thank all my colleagues at CFD lab for their help and cooperation. I am thankful to Dalton, Shaligram, Sudipta Basu, Ajay, Srinivas, PLN, Suman Basu, Debad, Ratnesh, Prabhakar, Jawahar and Neetu.

But for the constant encouragement of my friends I would not have completed this work. I shall be always grateful to those invisible persons whose support cannot be expressed in words.

November, 2001

I I T Kanpur

*Aseem Jain*

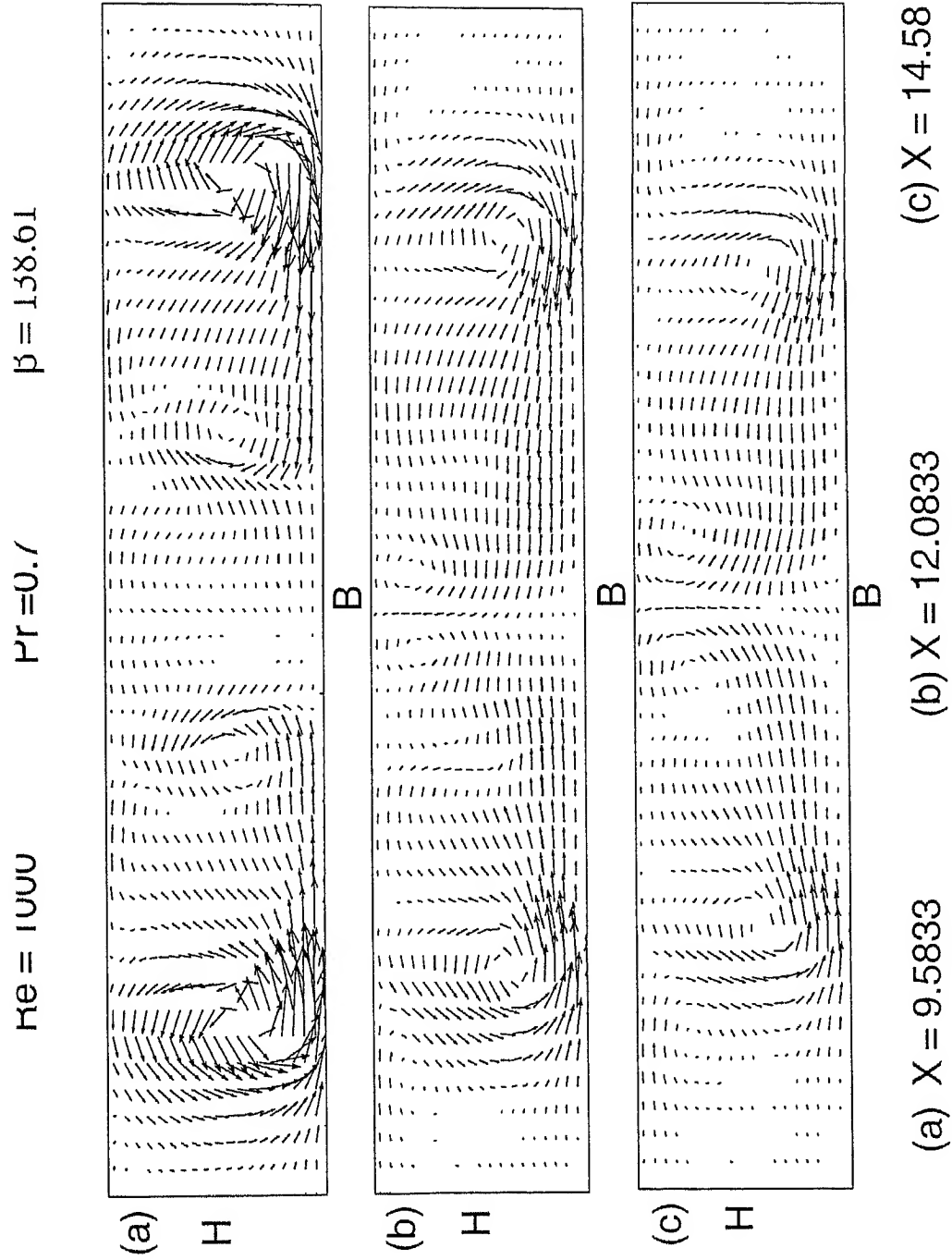


Figure 5.9 Cross-stream velocity vectors at different x-locations behind the delta winglet-pair ( $b/D=1.67$ )

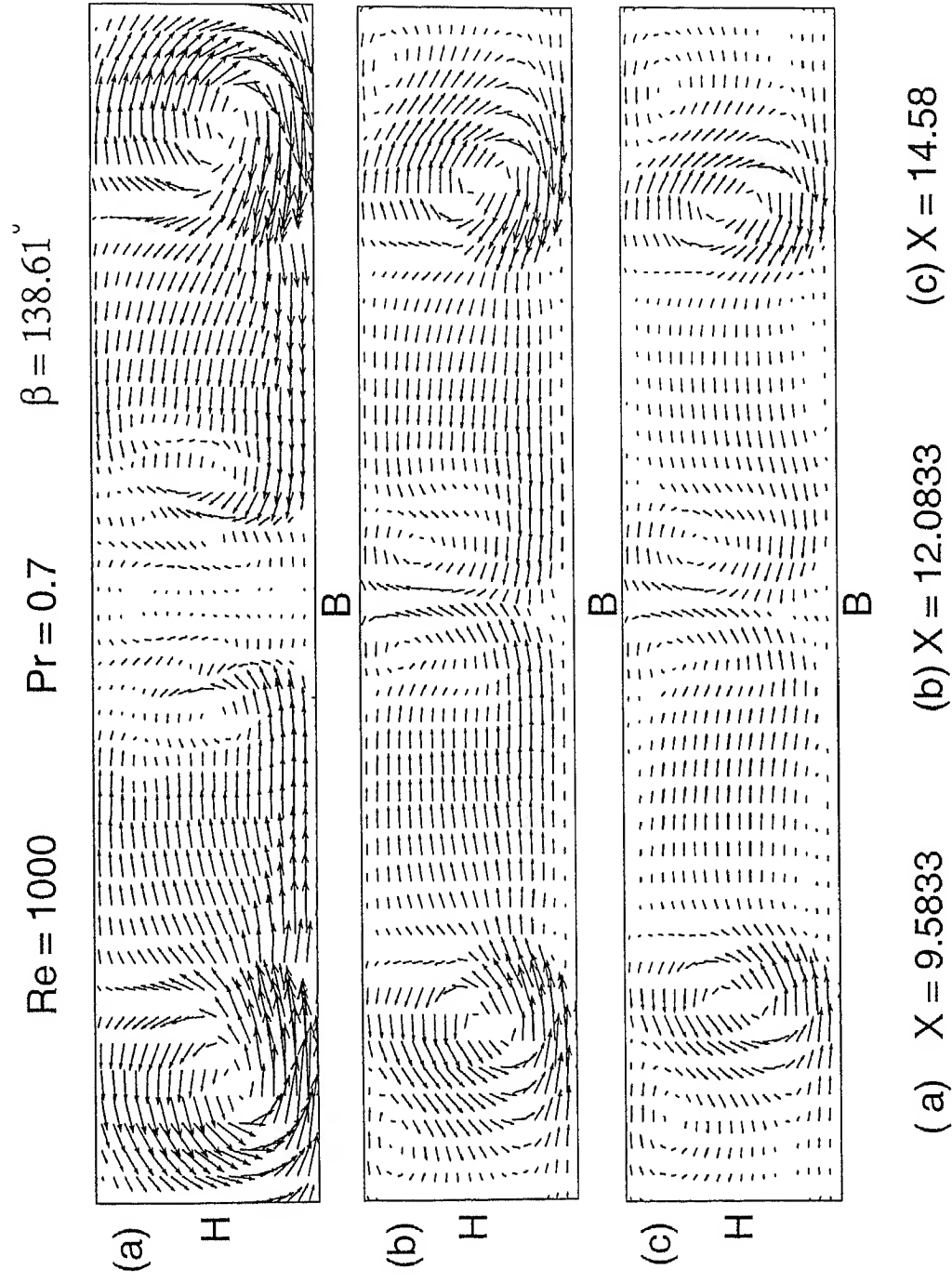


Figure 5.10 Cross-stream velocity vectors at different x-locations behind the rectangular winglet-pair



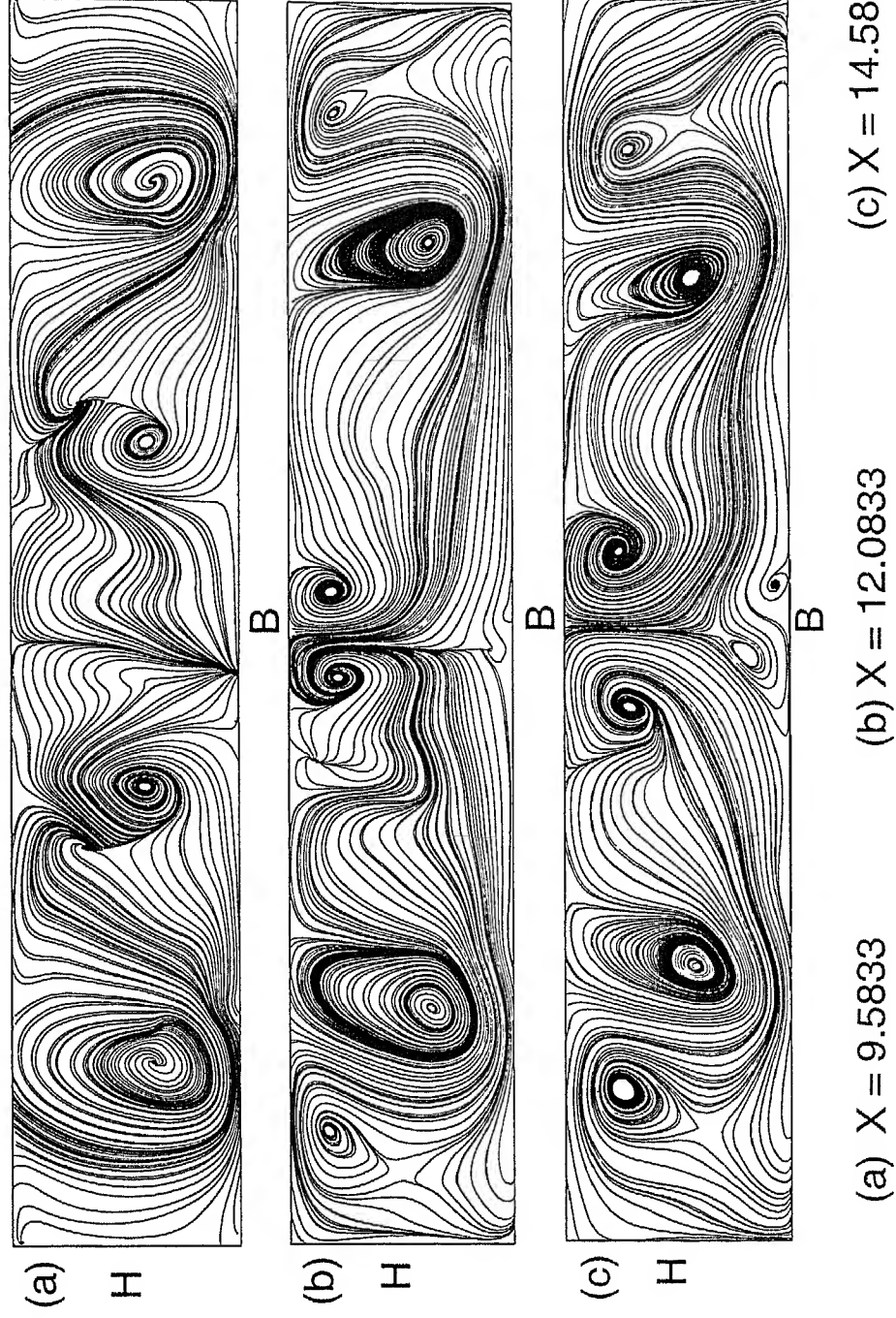


Figure 5.11 Streamlines on the cross-stream planes at different x-locations behind the delta winglet-pair ( $b/D=1.67$ )

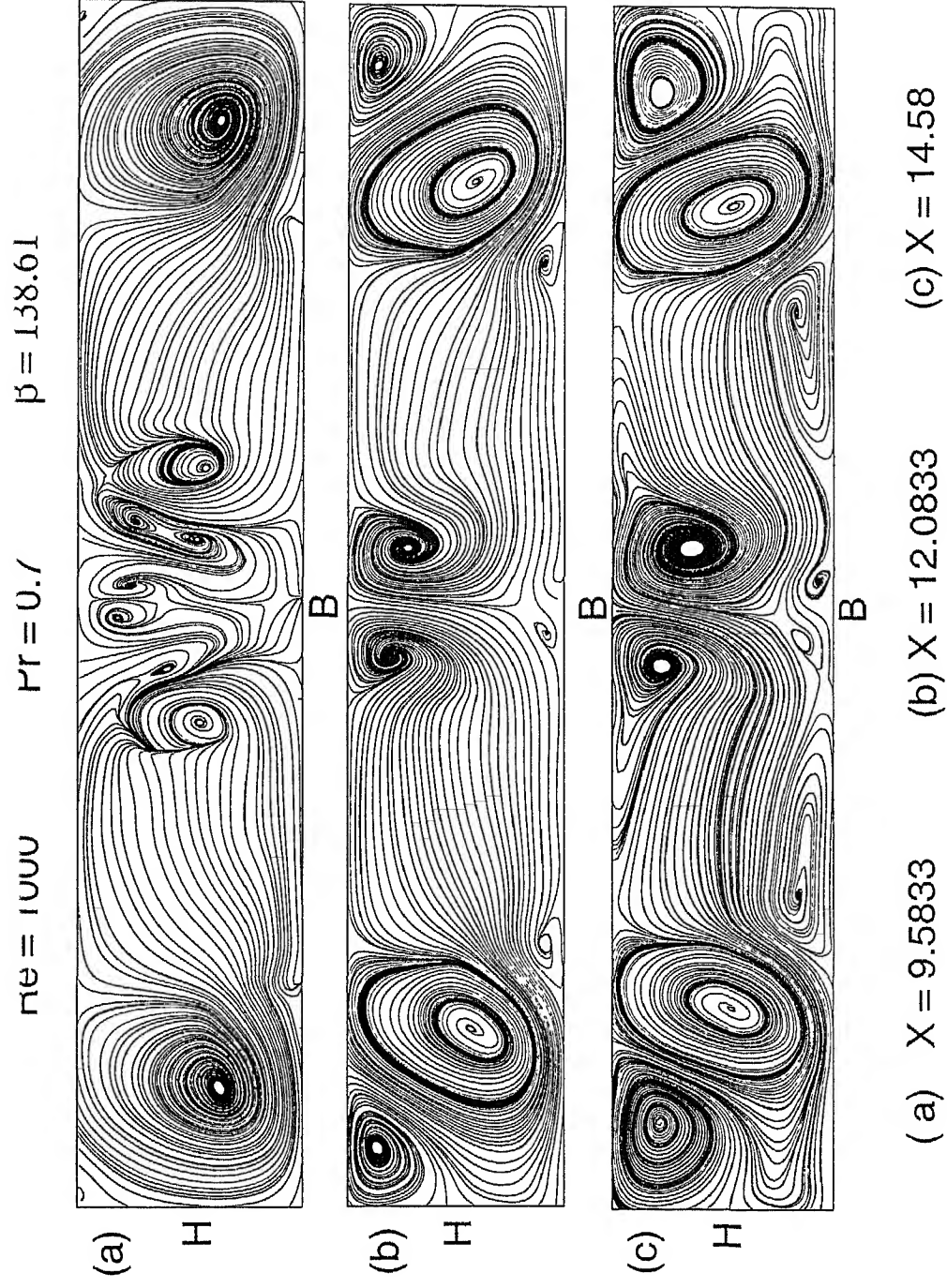


Figure 5.12 Streamlines on the cross-stream planes at different x-locations behind the rectangular winglet-pair

$Re = 1000$        $Pr = 0.7$        $\beta = 138.61$

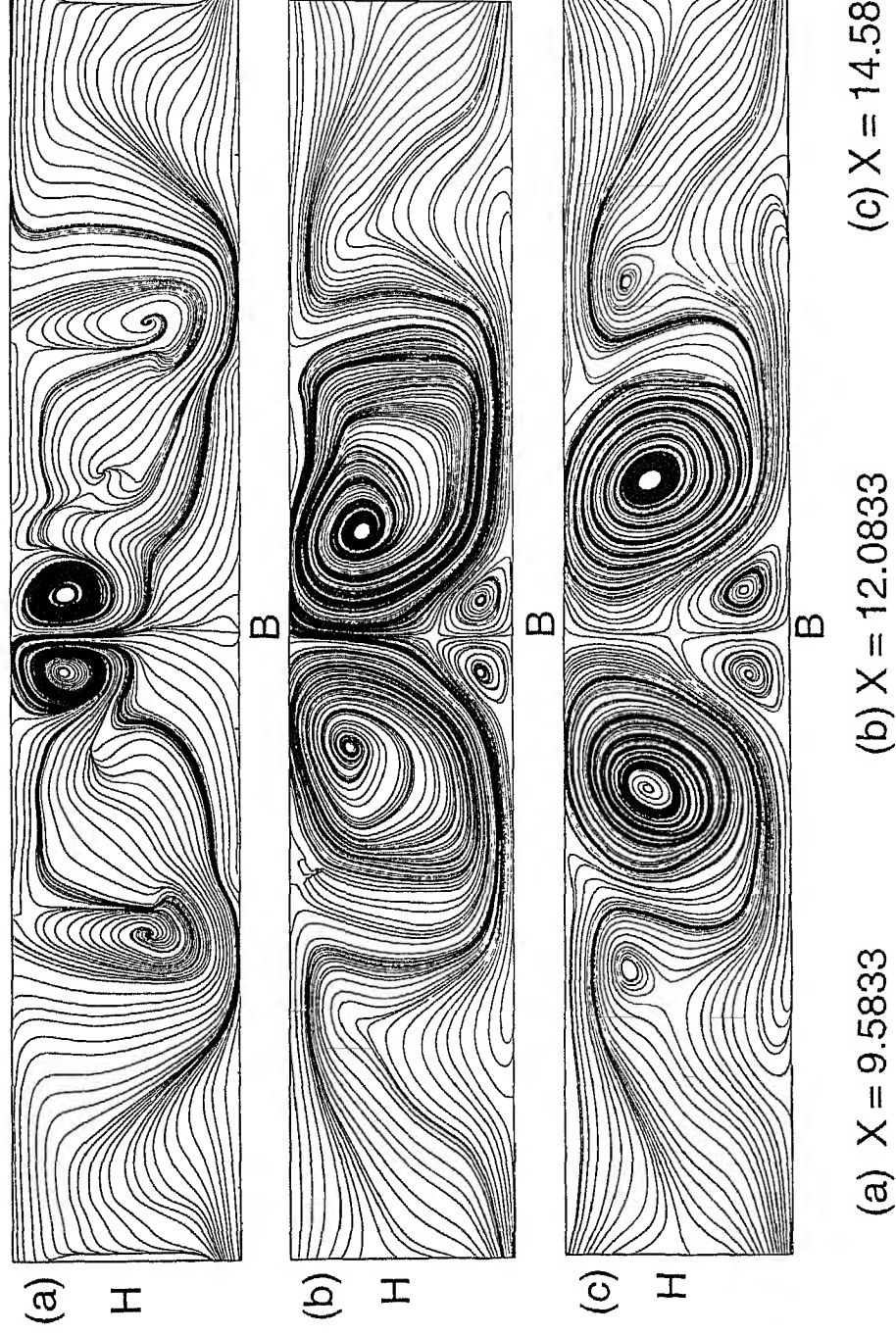


Figure 5.13 Streamlines on the cross-stream planes at different  $x$ -locations behind the delta winglet-pair

# Wake Region Behind Triangular Winglet In Common-Flow Up Configuration

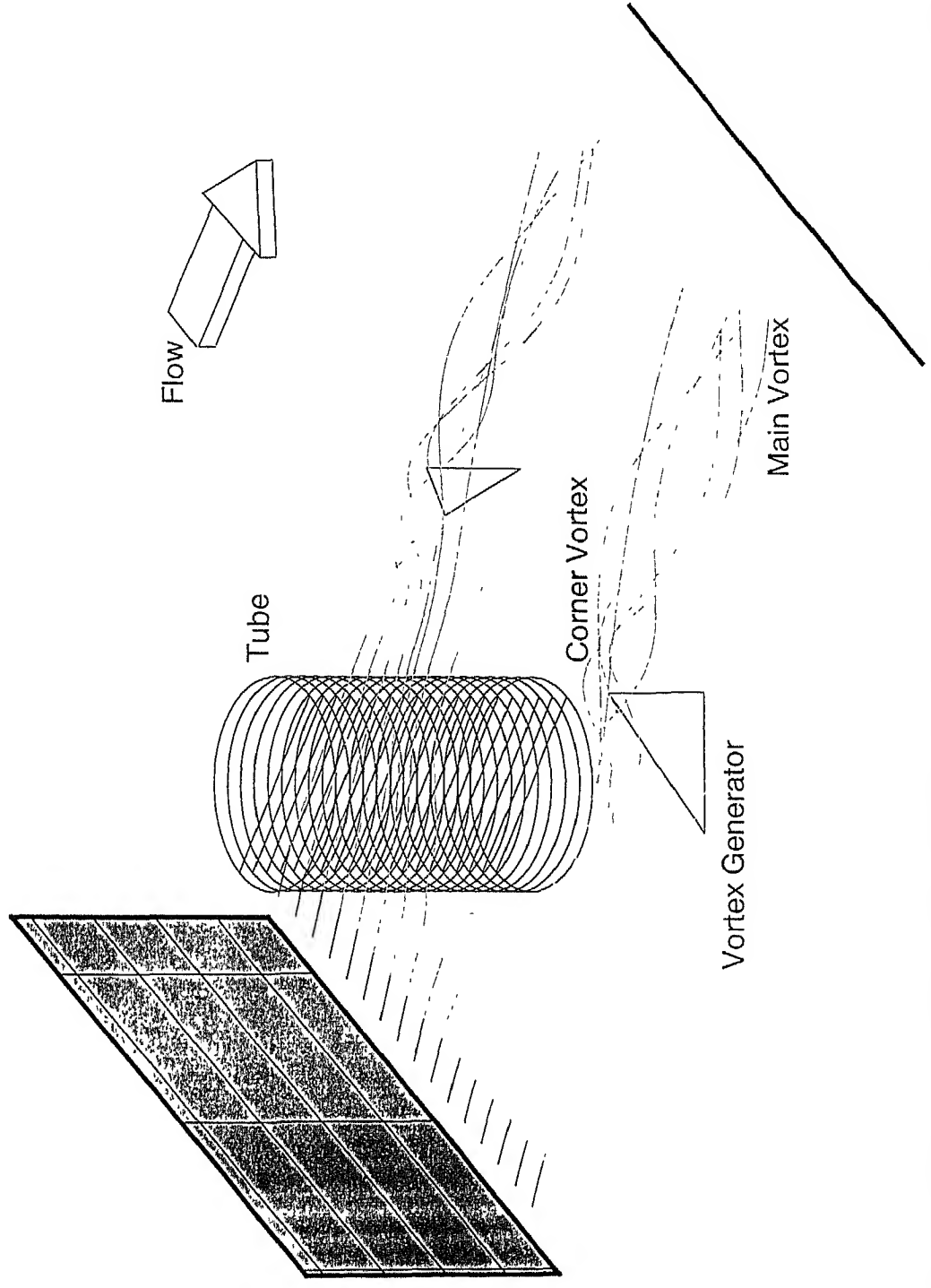


Figure 5.14 Three dimensional particle paths behind the delta winglet pair in common-flow-up configuration ( $b/D=1.67$ )

# Vortex formation with Tube and Winglet in Commonflow-up configuration

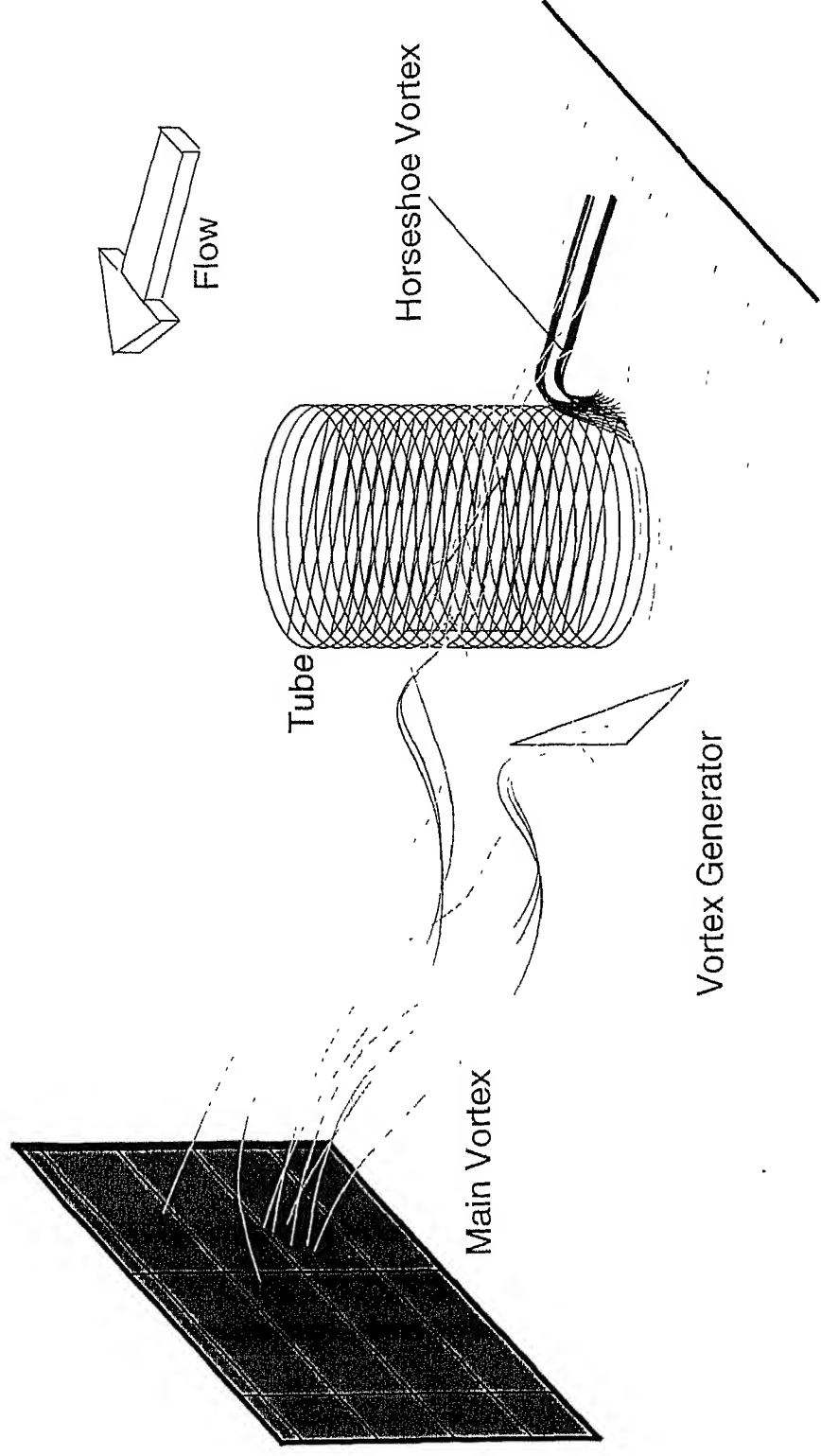
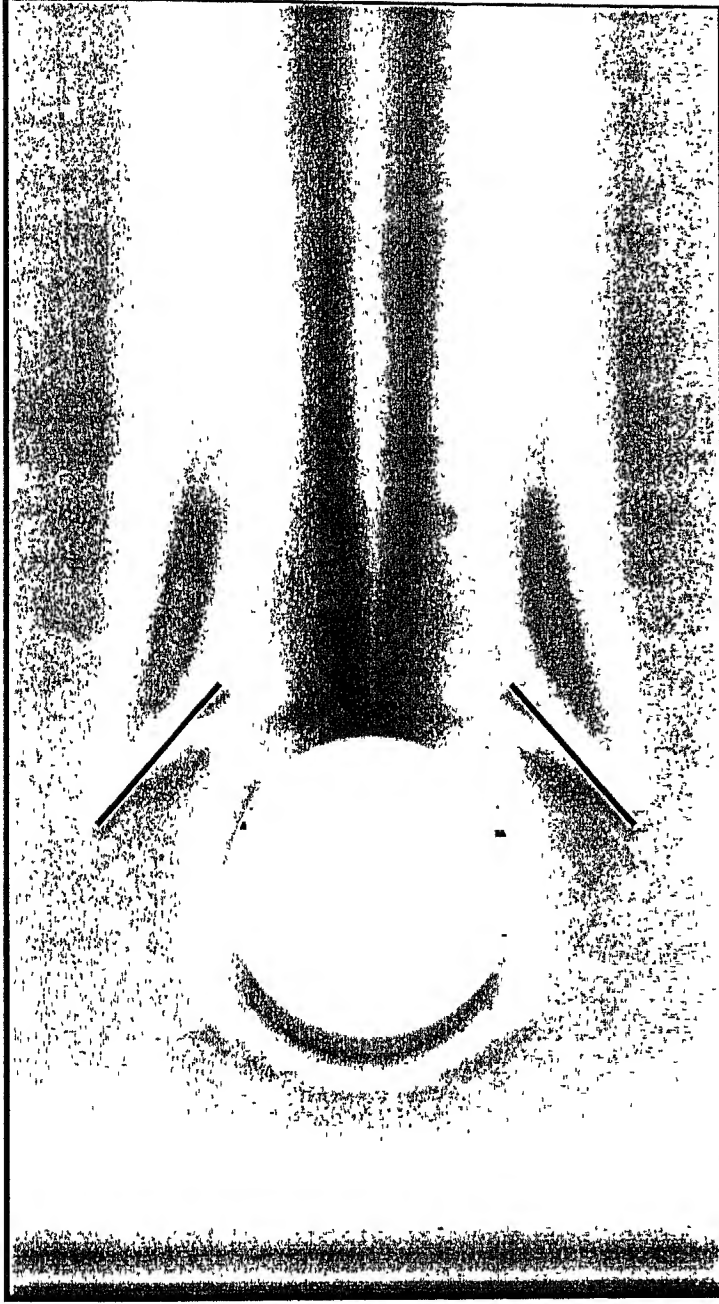


Figure 5.16 Three dimensional particle paths behind the delta winglet-pair in common-

flow-up configuration

$Re = 1000$ 
 $Pr = 0.7$ 
 $\beta = 138.61^\circ$



B

L

Nu



	0	4.51128	9.02256	13.5338	18.0451	22.5564	27.0677	31.5789
Nu								

Figure 5.17 Nusselt number distribution on the bottom plate of a channel with built-in circular tube and delta winglet-pair in common-flow-up configuration

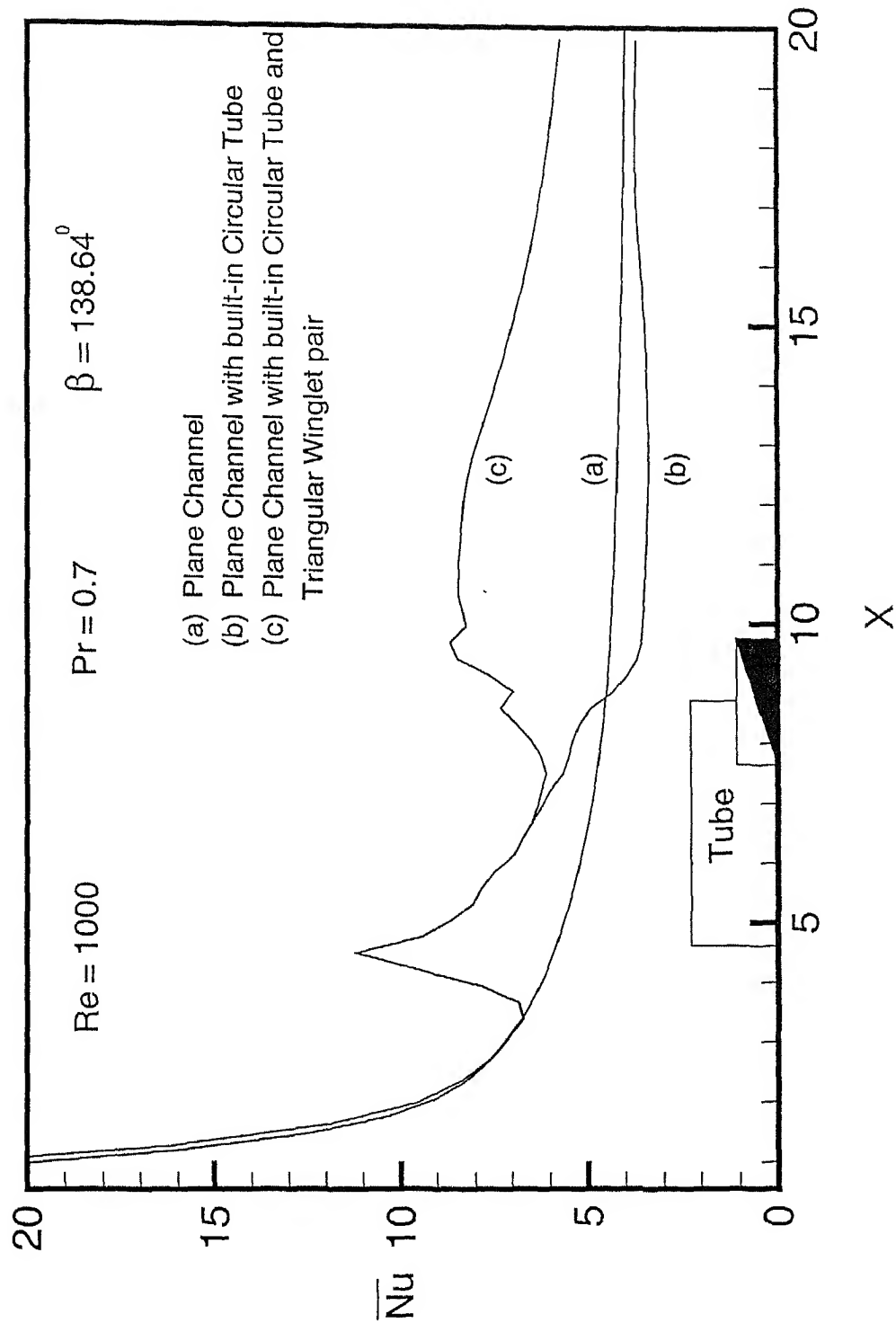


Figure 5.18  $\bar{Nu}$ , for a plane channel, channel with built-in circular-tube and channel with built-in circular-tube and delta winglet pair

# Contents

## List of figures

## Nomenclature

### 1 Introduction

1.1 Motivation	1
1.2 The Importance in Technology and Applications	1
1.3 Focused area and Specific Outline of the Present Problem	2
1.4 Layout of the Thesis	3

### 2 Literature Review

2.1 Introduction	6
2.2 Augmentation of Heat transfer	6
2.3 Literature on incompressible flow Modeling and Associated Heat Transfer Problems	8
2.4 Unsteady flows and Turbulence	10
2.5 How the Current Problem Benefits from Existing Literature	12

### 3 Formulation of the Problem

3.1 Introduction	15
3.2 Statement of the Problem	15
3.3 Governing Equations	16
3.4 Boundary Conditions	17

### 4 Grid Generation and Method of Solution

4.1 Introduction	19
4.2 Grid Generation	19
4.3 Computational Procedure for Grid Generation	20
4.4 Finite Volume Method	22



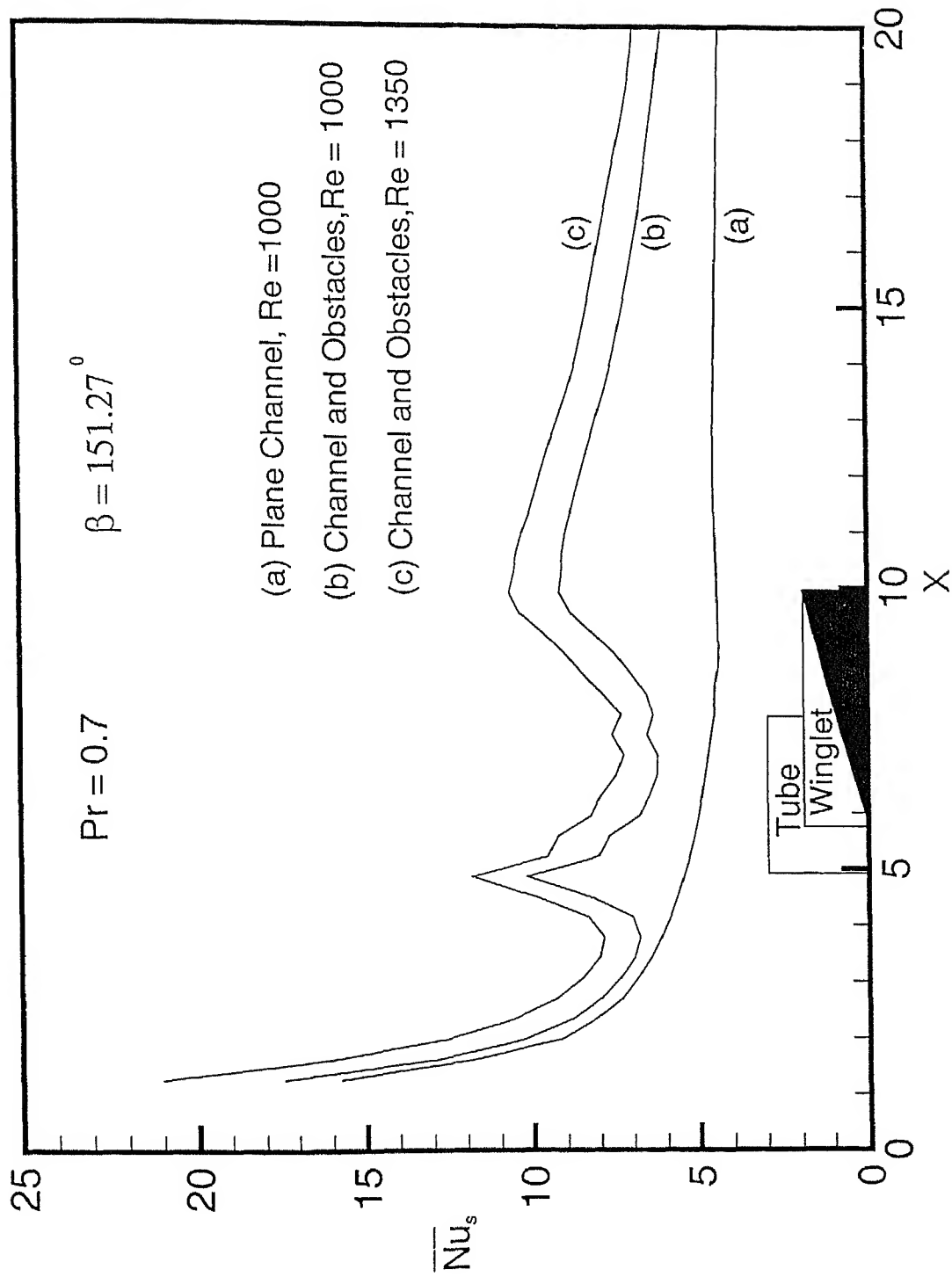


Figure 5.19 Span-averaged Nusselt number distribution for different Reynolds numbers

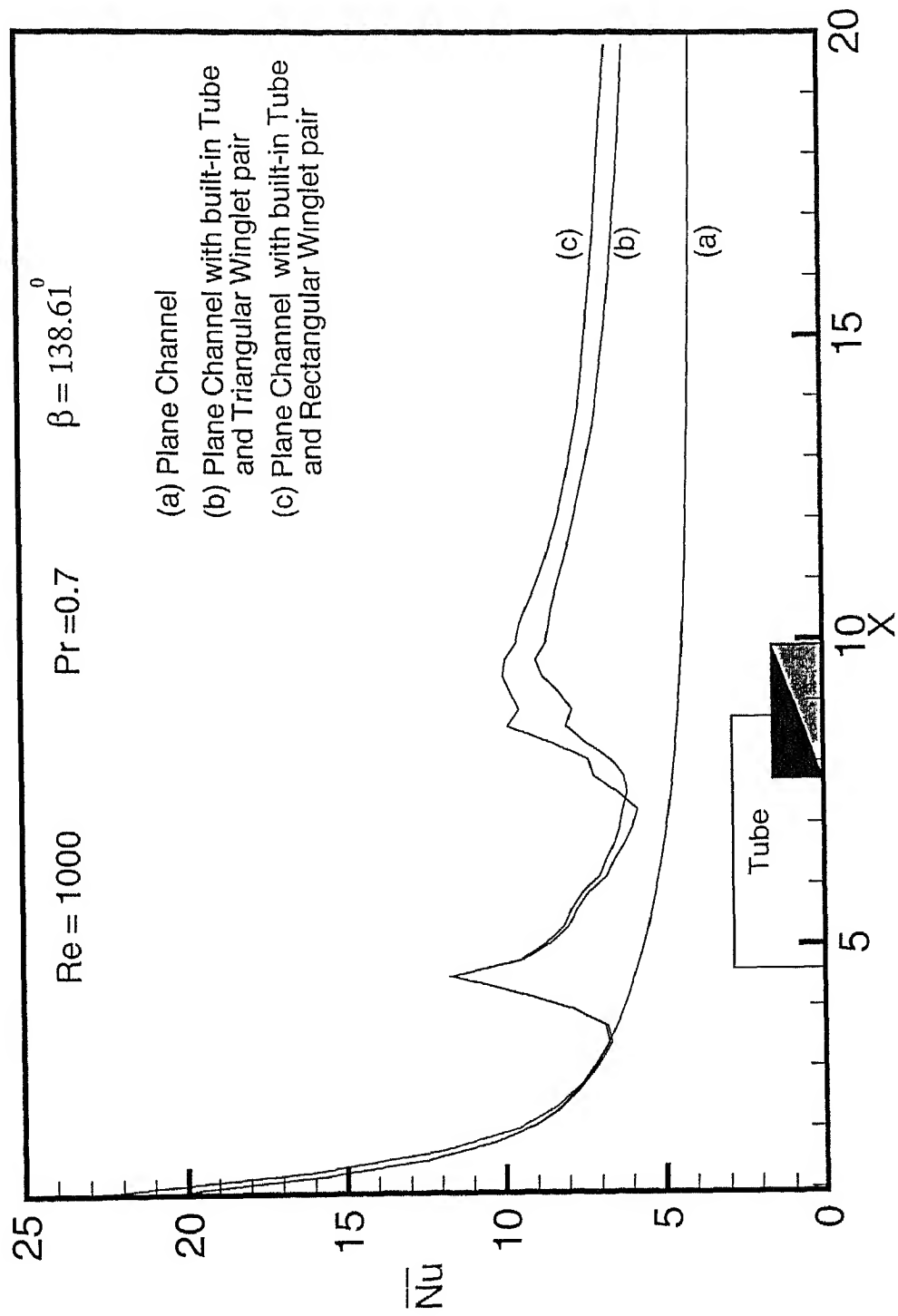


Figure 5.20  $\bar{Nu}_s$  for two different types of winglet-pair ( $b/D=1.67$ )

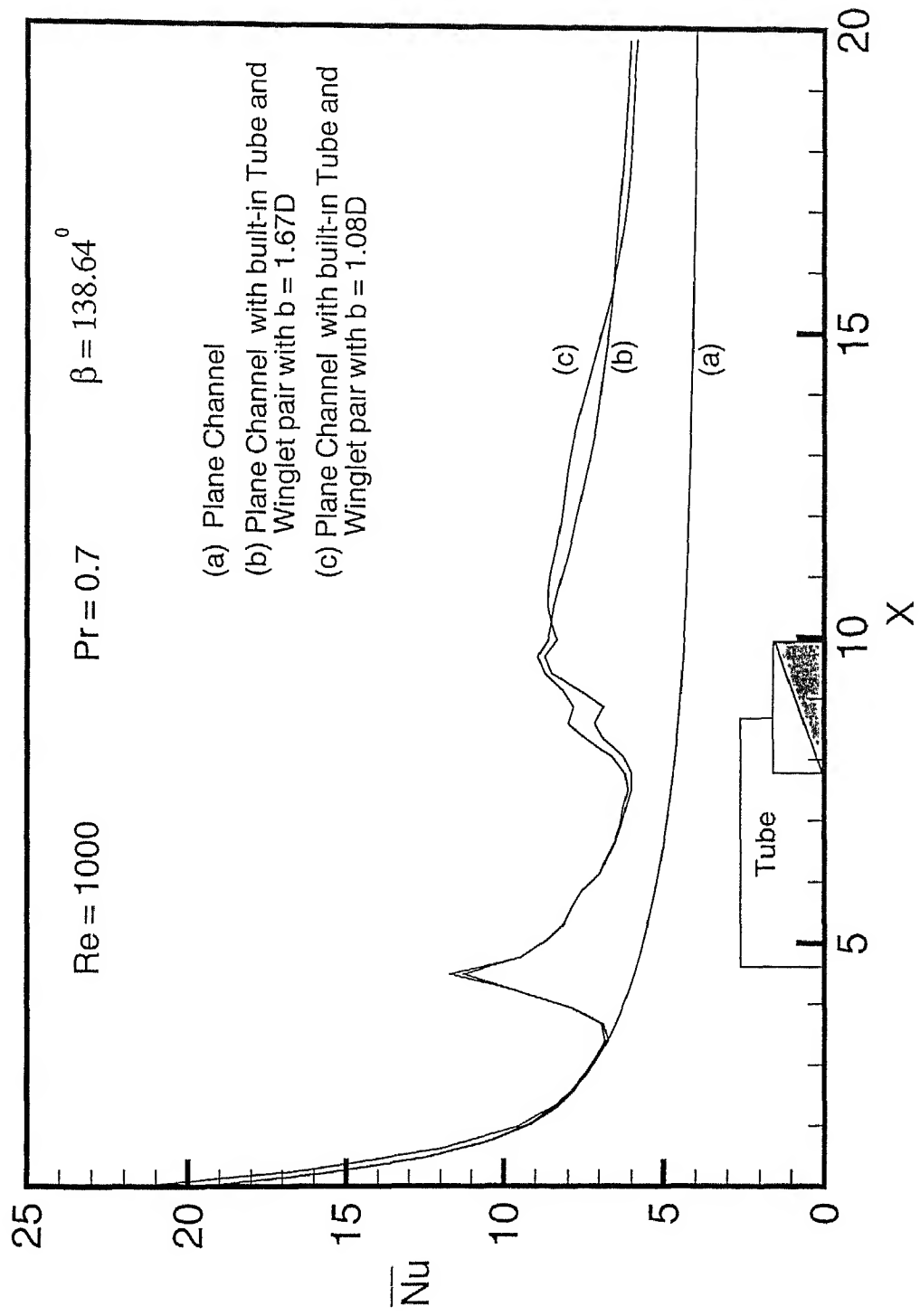


Figure 5.21  $\overline{Nu}_s$  for the delta winglet-pairs with different  $b/D$

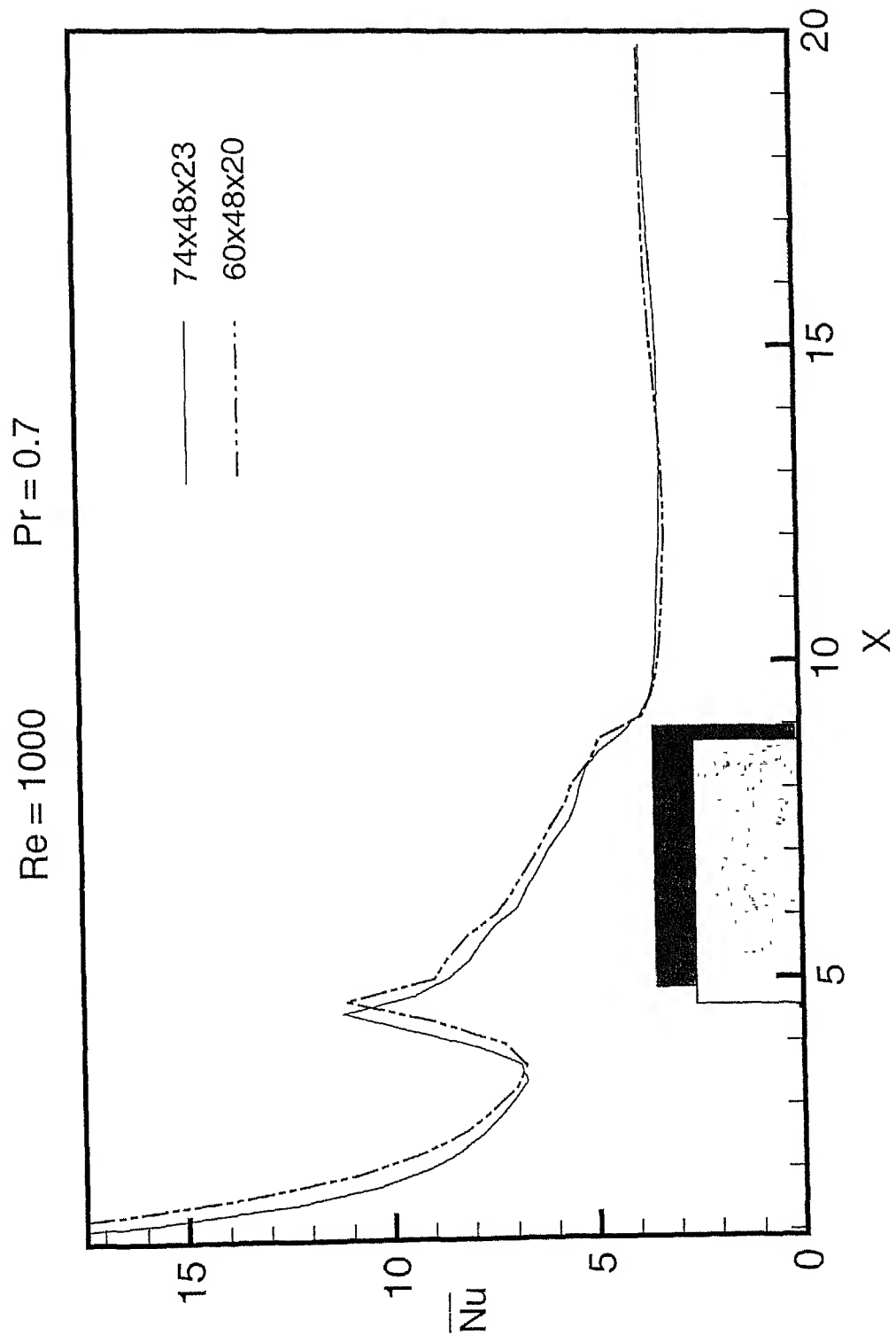


Figure 5.22 Grid independence test

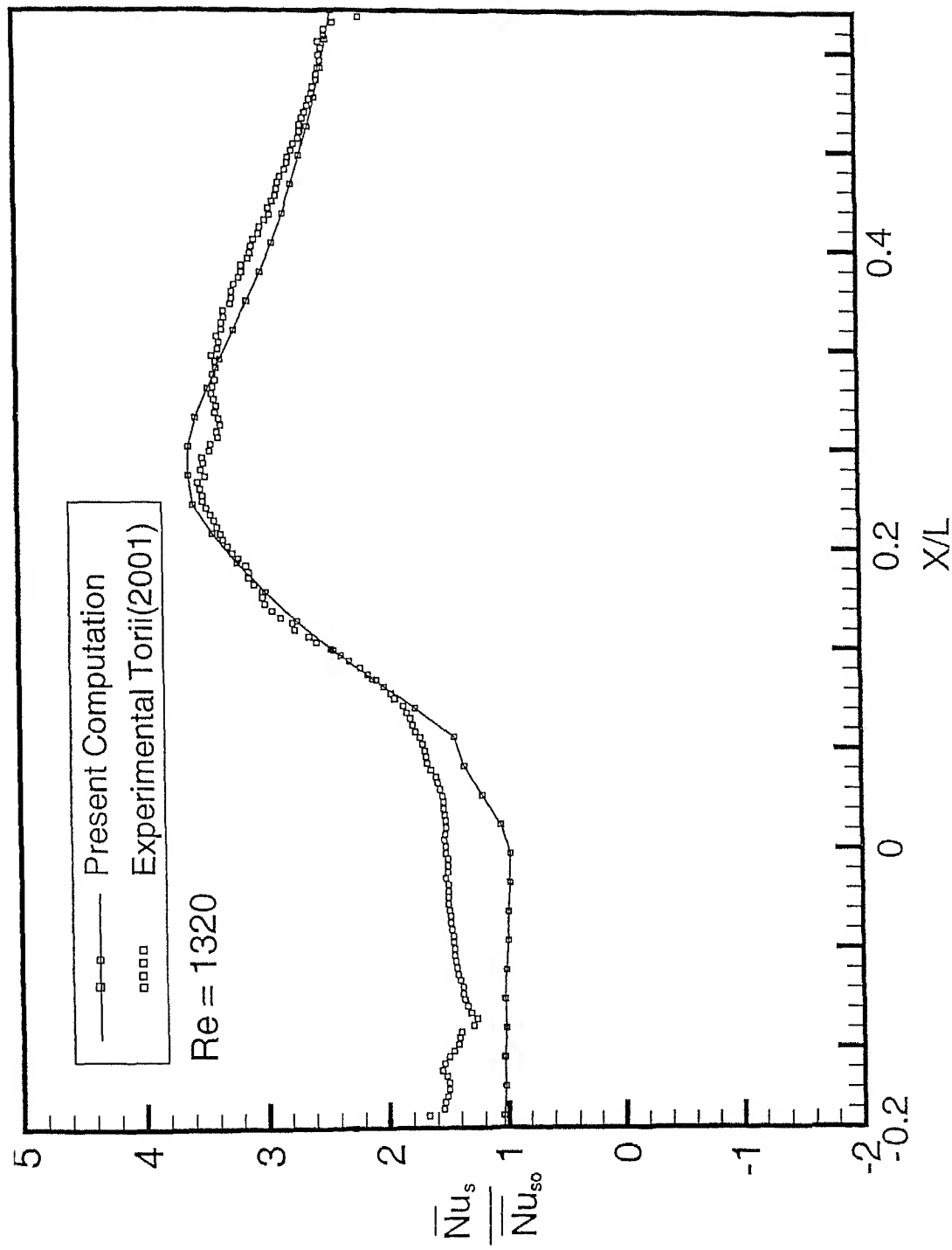


Figure 5.23 Comparison between the present computation and experimental results

### Conclusion and Scope for Future Work

#### 6.1 Concluding Remarks

A computational study has been accomplished to determine the flow structure and heat transfer in a rectangular channel with a built-in circular tube and different shaped vortex generators. The horseshoe vortices are generated at the junction of the forward stagnation line and the bottom plate. The horseshoe vortices travel in the downstream inducing a flow structure, which is primarily a longitudinal vortex system. However, this natural horseshoe vortex system does not persist in the downstream. Stronger longitudinal vortices are created by placing the winglet type vortex generators behind the circular tube. The present analysis reveals that the combination of circular tube and the winglet pair with common-flow-up configuration significantly improves the heat transfer performance. The nozzle like flow passages created by the winglet pair and the aft region of the circular tube promote accelerating flow and there by remove the zone of poor heat transfer from the near wake. At the end of a channel ( $X=20$ ) the span-averaged value of Nusselt number (based on channel height) is 5.8 for a Reynolds number of 1000. It may be mentioned that span-averaged Nusselt number (based on channel height) near the exit of a plane channel is 4.0 for the same Reynolds number. Enhancement of heat transfer is remarkable even at far downstream. The average Nusselt number of the entire bottom plate for the case of a channel with built in circular tube is 5.37 for a Reynolds number of 1000. The average Nusselt number of the plate improves to a value of 7.27 for the same Reynolds number when the winglet pair is added following the common-flow-up configuration.

## 6.2 Scope for Future Work

The results of this work reveal that the vortex generators with a common-flow-up configuration as a useful device for improving heat transfer in the air-cooled condensers for the geothermal power plants and other heat exchangers. The oval tubes can replace the circular tubes. This will reduce the form drag.

Here the computations have been done assuming flow regime to be laminar. Though turbulent flow is not frequently encountered in fin-tube heat exchangers, some special applications involving very high velocities, the flow regime can become turbulent. Therefore present study can be extended for the turbulent flows. Using an appropriate turbulence model, the performance of the proposed design can be computed for higher Reynolds numbers.

## References

1. Biswas, G. and Chattopadhyaya, H. (1992), Heat Transfer in a Channel with Built-in Wing-Type Vortex Generators, *Int. J. Heat Mass transfer*, Vol. 35, pp. 803-814.
2. Biswas, G., and Mitra, N. K. and Fiebig, M. (1994), Heat Transfer Enhancement in Fin-Tube Heat Exchangers by Winglet-Type Vortex Generators, *Int. J. Heat Mass Transfer*, Vol. 37, pp. 283-291.
3. Biswas, G., Deb, P., and Biswas, S., (1994), Generation of Longitudinal Streamwise Vortices - A Device for Improving Heat Exchanger Design, *Journal of Heat Transfer (ASME)*, Vol. 116, pp. 588-597.
4. Biswas, G., Torii, K., Fujii, D. and Nishino, K. (1996), Numerical and Experimental Determination of Flow Structure and Heat Transfer Effects of Longitudinal Vortices in a Channel Flow, *Int. J. Heat Mass Transfer*, Vol. 39, No. 16, pp. 3441-3451.
5. Cantwell, B. and Coles, D., (1983), An Experimental Study of Entrainment and Transport in the Turbulent Near Wake Circular Cylinder, *J. Fluid Mech.*, Vol. 136, pp. 321-374.
6. Eibeck, P.A. and Eaton, J.K. (1987), Heat Transfer of a Longitudinal Vortex Embedded in a Turbulent Boundary Layer, *Journal of Heat Transfer (ASME)*, Vol. 6, pp. 16-24.



7. Eswaran, V. and Prakash, S. (1998), A Finite Volume Method for Navier-Stokes Equations, *Proceedings of the third Asian CFD Conference, Bangalore*, Vol. 1, pp. 251-269.
8. Feigenbaum, M. J., (1980), The Onset Spectrum of Turbulence, *Phys. Lett.*, part-A, Vol. 74, pp. 375-378.
9. Ferziger, J. H., and Peric, M. (1999), *Computational Methods for Fluid Dynamics*, Springer Verlag, Berlin, New York
10. Fiebig, M., Kallweit, P. and Mitra, N. K. (1986), Wing Type Vortex Generators for Heat Transfer Enhancement, *Proc. 8<sup>th</sup> IHTC*, Vol. 6, pp. 2909-2913.
11. Fiebig, M., Brockmeier, U., Mitra, N. K. and Guntermann, T. (1989), structure of Velocity and Temperature Fields in Laminar Channel Flows with Longitudinal Vortex Generators, *Numerical Heat Transfer*, Part A, Vol. 15, pp. 281-302
12. Fiebig, M., Dong, Y. and Mitra N.K. (1990), Wärmeübergangserhöhung und Widerstandsverringern durch Längswirbelerzeuger in Rippenrohren, *Wärme und Stoffübertragung*, Vol. 25, pp. 34-44.
13. Fiebig, M., Kallweit, P., Mitra, N. K. and Tiggelbeck, S. (1991), Heat Transfer Enhancement and Drag by Longitudinal Vortex Generators in Channel Flow, *Experimental Thermal and Fluid Science*, Vol. 4, pp. 103-114.
14. Garg, V. K. and Maji, P. K. (1987), Flow through a Converging-Diverging Tube with Constant Wall Enthalpy, *Numerical Heat Transfer*, Vol. 12, pp. 285-305.

15. Gentry, M. C., Jacobi, A. M. (1997) , Heat Transfer Enhancement by Delta-Wing Vortex Generators on a Flat Plate: Vortex Interactions with Boundary Layer, *Experimental Thermal and Fluid Science*, Vol. 14, pp. 231-242
16. Goldstein, R. J. and Karni, J.(1984), The Effect of a Wall Boundary Layer on a Local Mass Transfer from a Cylinder in Crossflow, *Journal of Heat Transfer (ASME)*, Vol. 106,pp.260-267
17. Guzmán, A. M. and Amon, C. H., (1996), Dynamical Flow Characterization of Transitional and Chaotic regimes in Converging-Diverging Channels, *J. Fluid Mech.*, Vol. 321, pp. 25-57.
18. Harlow, F. H., and Welch, J. E., (1965), Numerical Calculation of Time-dependent Viscous Incompressible Flow of Fluid with Free Surface, *The Phys. Fluids*, Vol. 8, pp. 2182-2188.
19. Hirt, C. W. and Cook, J. L. (1972), Calculating Three-Dimensional Flows Around Structures and Over Rough Terrain, *J. Comp. Phys.*, Vol. 10, pp. 324-340.
20. Khosla, P. K., and Rubin, S. G., (1974), A diagonally dominant second-order accurate implicit scheme, *Comp. & Fluids*, Vol. 2, pp. 207-209.
21. Kordulla, W., and Vinokur, M., (1983), Efficient Computation of Volume in Flow Predictions, *AIAA J.*, Vol. 21, No. 6, pp. 917-918.
22. Kobayashi, M.H. and Pereira, C.F. (1991), Calculation of Incompressible Laminar Flows on a Non-Staggered, Non-Orthogonal Grid, *Numerical Heat Transfer*, Part B, Vol. 19, pp. 243-262.

4.5 Surfaces areas and Volumes	23
4.6 Discretization Procedure	23
4.6.1 Discretization of Continuity Equation	24
4.6.2 Discretization of General Equation	24
4.7 Pressure-Velocity Coupling	31
4.8 Solution Algorithm	34
4.9 Numerical Stability Considerations	36
<b>5 Results and Discussion</b>	
5.1 Introduction	41
5.2 Flow and Heat Transfer Characteristics in a Rectangular Channel with a built-in Circular Tube	41
5.2.1 Flow Characteristics	41
5.2.1 Heat Transfer Characteristics	42
5.3 Effect of Winglet-Pair on Flow and Heat Transfer	43
5.3.1 Flow Characteristics	43
5.3.2 Heat Transfer Characteristics	45
5.4 Spatial Grid Independence Model Validation	47
<b>6 Conclusion and Scope for Future Work</b>	
6.1 Concluding Remarks	72
6.2 Scope for future work	73
<b>7 References</b>	74

23. Majumdar, S., Rodi, W., and Zhu, J., 1992, Three-Dimensional Finite-Volume Method for Incompressible flows with Complex Boundaries, *J. of Fluids Engg. (ASME)*, Vol. 114, pp. 496-503.
24. Majumdar, S. (1988), Role of Underrelaxation in Momentum Interpolation for calculation of Flow with Non-Staggered Grids, *Numerical Heat Transfer*, Vol. 13, pp. 125-132.
25. Manneville, P. and Pomeau, Y. (1980), Different ways to Turbulent in Dissipative Dynamical Systems, *Physica D*, Vol. 1, pp. 219-226.
26. Mendez, R. R., Sen, M., Yang, K. T. and McClain, R. L. (1998), Enhancement of Heat transfer in an Inviscid-Flow Thermal Boundary layer Due to a Rankine Vortex, *Int. J. Heat Mass Transfer*, Vol. 41, pp. 3829-3840.
27. Mochizuki, S., Yogi Y. and Yang W. J. (1988), Advances in Single-Blow Method for Performance Evaluation of Heat Transfer Surfaces, *Proc. of 2<sup>nd</sup> Int. Symp. On Heat Transfer*, pp. 284-291, Beijing, China.
28. Mukhopadhyay, A., Sundarajan, T. and Biswas, G. (1993), An Explicit Transient Algorithm for Predicting Incompressible Viscous Flows in Arbitrary Geometry, *Int. J. of Heat Transfer*, Vol. 114, pp. 280-284.
29. Nichols, B. D. and Hirt, C. W., (1971), Improved Free Surface Boundary Conditions for Numerical Incompressible Calculations, *J. Compt. Phys.*, Vol. 8, pp. 434-448.
30. Orlanski, I. (1976), A Simple Boundary Condition for Unbounded Flows, *J. Comp. Phys*, Vol. 21, pp. 251-269.

31. Patankar, S. V. and Spalding, D. B. (1972), A Calculation Procedure for Heat Mass and Momentum Transfer in three-Dimensional Parabolic Flows, *Int. J. Heat Mass Transfer*, Vol. 15, pp. 1787-1806.
32. Patankar, S. V. (1981), A Calculation Procedure for Heat and Momentum Transfer in Three-Dimensional Parabolic Flows, *Int. J. Heat Mass Transfer*, Vol. 15, pp. 1787-1806.
33. Pauley, W. R. and Eaton, J. K. (1988), Experimental Study of the Development of Longitudinal Vortex pairs Embedded in a Turbulent Boundary Layer, *AIAA J.*, Vol. 26, pp. 816-823.
34. Peric, M. (1985), A Finite Volume Method for the Prediction Of Three-Dimensional Fluid Flow in Complex Ducts, *Ph. D. Thesis*, University of London.
35. Peric, M., Kessler, R. and Scheuerer, G. (1988), Comparison of Finite-Volume Numerical Methods with a Staggered and Collocated Grids, *Computers & Fluids*, Vol. 16, pp. 389-403.
36. Pulliam, T. H. and Vastano, J. A., (1993), Transition to chaos in an Open Unforced 2D Flow, *J. Comput. Phys.*, Vol. 96, pp. 15-53.
37. Robichaux, J., Tafti, D. K. and Vanka, S. P., (1992), Large Eddy Simulations of Turbulence on the CM-2, *Numerical Heat Transfer*, Part-B, Vol. 21, pp. 367-388.
38. Ruelle, D. and Takens, F., (1971), On the Nature of turbulence, *Commun. Math. Phys.*, Vol. 20, pp. 167-192.
39. Rhie, C. M. and Chow, B. L. (1983), Numerical Study of Flow Past an Aerofoil with Trailing Edge Separation, *AIAA J.*, Vol. 21, pp. 1525-1532.

40. Rhie, C. M. (1981), A Numerical Study of the Flow Past an Isolated Airflow with Separation, Ph.D. Thesis, Dept. of Mechanical and Industrial Engg., University of Illinois at Urbana Champaign, 1981.
41. Sanchez, M., Mitra, N. K. and Fiebig, M. (1989), Numerical Investigations of Three-Dimensional Laminar Flows in a Channel with Built-In Circular Cylinder Wing-Type Vortex Generators. *Proc. Eighth GAMM-Conference on numerical methods*, Vieweg Verlag, pp. 484-492
42. Tiggelbeck, S., Mitra, N. K., and Fiebig, M., (1994), Comparison of Wing Type Vortex Generators for Heat Transfer Enhancement in Channel Flows, *Journal of Heat Transfer (ASME)*, Vol. 116, pp. 880-885.
43. Torii K., Nishino K. M., Kwak K. M., and Kawai R. (2000), YNU Team Report: Research Results and Implementation Plan, NEDO VORTEX Team Meeting.
44. Torii K., (2001) Personal Communications.
45. Turk, A. J. and Junklan, G. H. (1986), Heat Transfer Enhancement Downstream of Vortex Generators on a Flat Plate, *Proc. 8<sup>th</sup> IHTC*, Vol 6 , pp. 2903-2908, San Francisco
46. Tsai, S. F., Sheu, T. W. H. and Lee, S. M. (1999), Heat transfer in a conjugate heat exchanger with a wavy fin surface, *Int. J. Heat Mass Transfer*, Vol. 42, pp. 1735-1745.
47. Valencia, A., Fiebig, M., and Mitra, N. K., (1996) Heat Transfer Enhancement by Longitudinal Vortices in Fin-Tube Heat Exchanger Element with Flat Tubes, *Journal of Heat Transfer (ASME)*, Vol. 118, pp 209-211.

48. Van Doormal, J. P., and Raithby, G. D., (1984), Enhancement of SIMPLE method of Predicting Incompressible Fluid Flows, *Numerical Heat Transfer*, Vol. 7, pp 147-163.
49. Verma, A. K. and Eswaran, V.(1996), Overlapping Control Volume Approach for Convection-Diffusion Equation, *Int. J. Numerical Methods Fluids*, Vol. 23,pp. 865-882.
50. Verma A. K., and Eswaran, V.(1997), A Bounded Convection Scheme for the Overlapping Control Volume Approach, *Int. J. Numerical Methodes Fluids*
51. Vittori, G. and Blondeaux, P. (1993), Quasiperiodicity and Phase Locking Route to chaos in the Two-Dimensional Oscillatory Flow Around a Circular Cylinder, *Phys. Fluids*, Part-A, Vol. 5, pp. 1866-1868.
52. Westphal, R. V., and Mehta, R. D., 1987, Interaction of Oscillating Vortex with a Turbulent Boundary layer, *AIAA 19<sup>th</sup> Fluid Dynamics and Laser Conference*, Hawaii, AIAA paper no. 87-1246.
53. Yanagihara, J. L. and Torii, K., (1990), Heat Transfer characteristics of Laminar Boundary Layer in the Presence of Vortex Generators, *Proc9<sup>th</sup> IHTC*, Vol. 6, pp.323-328.

A' 141972





## List of Figures

Figure 1.1	Schematic diagram of core region of a fin-tube heat exchanger	4
Figure 1.2	Delta-winglet type vortex generators on flat surface	4
Figure 1.3	Heat exchanger module considered in present investigation	5
Figure 2.1	Element of existing fin-tube heat exchanger	14
Figure 4.1	Schematic of the grid-mesh and the computational domain	37
Figure 4.2	Three-dimensional finite volume cell	38
Figure 4.3	Face representation to illustrate diffusion model	39
Figure 4.4	Flowchart of iterative solution scheme	40
Figure 5.1(a)	Limiting streamlines based on instantaneous flow on a plane close to the bottom plate for a channel with built-in circular tube	48
(b)	Limiting streamlines based on time-averaged flow on a plane close to the bottom plate for a channel with built-in circular tube	49
Figure 5.2	Vortex shedding at the mid-plane in the wake of a circular tube (shedding starts from the bottom side of the tube).	50
Figure 5.3	Vortex shedding at the mid-plane in the wake of a circular tube (shedding starts from the top side of the tube).	51
Figure5.4	Streamline-plot for time-averaged flow on a horizontal mid-plane of the channel with a built-in circular tube	52